

1
2 **The oral drug nitazoxanide restricts SARS-CoV-2 infection and attenuates**
3 **disease pathogenesis in Syrian hamsters**
4

5
6 §Lisa Miorin^{1,2,#}, Chad E. Mire^{3,#}, Shahin Ranjbar^{4,#},
7 Adam J. Hume^{5,6}, Jessie Huang^{7,8}, Nicholas A. Crossland^{5,9}, Kris M White^{1,2}, Manon Laporte^{1,2},
8 Thomas Kehrer^{1,2}, Viraga Haridas⁴, Elena Moreno^{1,2}, Aya Nambu⁴, Sonia Jangra^{1,2},
9 Anastasija Cupic^{1,2}, Marion Dejosez¹⁰, Kristine A. Abo^{7,8}, Anna E. Tseng^{5,9},
10 Rhiannon B. Werder^{7,8}, Raveen Rathnasinghe^{1,2}, Tinaye Mutetwa¹, Irene Ramos¹,
11 Julio Sainz de Aja¹¹, Carolina Garcia de Alba Rivas¹¹, Michael Schotsaert^{1,2}, Ronald B. Corley^{5,9},
12 James V. Falvo⁴, Ana Fernandez-Sesma¹, Carla Kim^{11,12,13}, Jean-François Rossignol¹⁴,
13 Andrew A. Wilson^{7,8}, Thomas Zwaka¹⁰, Darrell N. Kotton^{7,8,9}, Elke Mühlberger^{5,6},
14 Adolfo García-Sastre^{1,2,15,16,17}, §Anne E. Goldfeld^{4,18,19}
15

16 ¹Department of Microbiology, Icahn School of Medicine at Mount Sinai, New York, NY, USA; ²Global Health
17 Emerging Pathogens Institute, Icahn School of Medicine at Mount Sinai, New York, NY, USA; ³University
18 of Texas Medical Branch, Galveston, TX, USA; ⁴Program in Cellular and Molecular Medicine, Boston
19 Children's Hospital, Harvard Medical School, Boston, MA, USA; ⁵National Emerging Infectious Diseases
20 Laboratories, Boston University, Boston, MA, USA ⁶Department of Microbiology, Boston University School
21 of Medicine, Boston, MA, USA; ⁷Center for Regenerative Medicine of Boston University and Boston Medical
22 Center, Boston, MA, USA; ⁸The Pulmonary Center and Department of Medicine, Boston University School
23 of Medicine, Boston, MA, USA; ⁹Department of Pathology and Laboratory Medicine, Boston University
24 School of Medicine, Boston, MA, USA; ¹⁰Cell, Developmental & Regenerative Biology, Icahn School of
25 Medicine at Mount Sinai; New York, NY, USA; ¹¹Stem Cell Program, Boston Children's Hospital, Boston,
26 MA, USA; ¹²Harvard Stem Cell Institute, Cambridge, Massachusetts; ¹³Department of Genetics, Harvard
27 Medical School, Boston, MA, USA; ¹⁴Romark Institute for Medical Research, Tampa, FL, USA; ¹⁵Department
28 of Medicine, Division of Infectious Diseases, Icahn School of Medicine at Mount Sinai, New York, NY, USA;
29 ¹⁶Tisch Cancer Institute, Icahn School of Medicine at Mount Sinai, New York, NY, USA; ¹⁷Department of
30 Pathology, Molecular and Cell-Based Medicine, Icahn School of Medicine at Mount Sinai, New York, NY,
31 USA; ¹⁸Division of Infectious Diseases, Department of Medicine, Brigham and Women's Hospital, Harvard
32 Medical School, Boston, MA, USA; ¹⁹Department of Immunology and Infectious Diseases, Harvard T.C.
33 Chan School of Public Health, Boston, MA, USA.
34
35

36 #These authors contributed equally

37 §To whom correspondence should be addressed:

38 Lisa Miorin: lisa.miorin@mssm.edu; Anne E. Goldfeld: anne.goldfeld@childrens.harvard.edu
39

40 **Abstract**

41

42 A well-tolerated and cost-effective oral drug that blocks SARS-CoV-2 growth and
43 dissemination would be a major advance in the global effort to reduce COVID-19 morbidity and
44 mortality. Here, we show that the oral FDA-approved drug nitazoxanide (NTZ) significantly inhibits
45 SARS-CoV-2 viral replication and infection in different primate and human cell models including
46 stem cell-derived human alveolar epithelial type 2 cells. Furthermore, NTZ synergizes with
47 remdesivir, and it broadly inhibits growth of SARS-CoV-2 variants B.1.351 (beta), P.1 (gamma),
48 and B.1617.2 (delta) and viral syncytia formation driven by their spike proteins. Strikingly, oral
49 NTZ treatment of Syrian hamsters significantly inhibits SARS-CoV-2-driven weight loss,
50 inflammation, and viral dissemination and syncytia formation in the lungs. These studies show
51 that NTZ is a novel host-directed therapeutic that broadly inhibits SARS-CoV-2 dissemination and
52 pathogenesis in human and hamster physiological models, which supports further testing and
53 optimization of NTZ-based therapy for SARS-CoV-2 infection alone and in combination with
54 antiviral drugs.

55

56

57

58

59

60

61

62 **Keywords:** SARS-CoV-2; COVID-19; Delta variant; FDA-approved oral drug; Nitazoxanide, NTZ;
63 viral syncytia; Spike; type-I interferon; host-directed therapeutic; alveolar epithelial type 2 cells;
64 Syrian hamsters; imaging flow cytometry.

65

66 Introduction

67

68 The ongoing COVID-19 pandemic has resulted in more than 396 million cases and 5.7
69 million deaths worldwide (Dong et al., 2020). An easily deployable, well-tolerated, inexpensive,
70 orally active drug that is safe in adults and children to treat or inhibit disease progression would
71 be a significant advance in the fight against COVID-19. Nitazoxanide (NTZ) is an FDA-approved
72 and well-tolerated oral therapy originally developed for parasitic infection that has been used for
73 treatment of *Giardia*- and *Cryptosporidium*-associated diarrhea in millions of adults and children
74 (Dumbo et al., 1997; Hussar, 2004; Rossignol et al., 1998). In addition, both NTZ and its
75 circulating metabolite tizoxanide (TIZ) have been shown to inhibit a diverse array of viruses,
76 including human coronaviruses *in vitro* (Rossignol, 2014; Wang et al., 2020).

77 Our previous studies showed that NTZ functions as a host-directed therapeutic (HDT) that
78 inhibits Ebola virus (EBOV) and vesicular stomatitis virus (VSV) by amplifying host cytosolic RNA
79 sensing and type I interferon (IFN) signaling pathways and by inducing the cell stress and antiviral
80 phosphatase GADD34 (Jasenosky et al., 2019). These studies, which showed that NTZ creates
81 a broad “antiviral milieu” capable of overcoming virus-specific immune evasion strategies
82 (Jasenosky et al., 2019; Ranjbar et al., 2019), led us to test NTZ’s ability to inhibit severe acute
83 respiratory syndrome coronavirus 2 (SARS-CoV-2) replication and pathogenesis in
84 physiologically relevant preclinical models of infection.

85 Here, we show that NTZ significantly inhibits SARS-CoV-2 replication in human and
86 primate cell lines including human alveolar epithelial type 2 cells (iAT2s) derived from induced
87 pluripotent stem cells (iPSCs). We also show that NTZ broadly inhibits replication of SARS-CoV-
88 2 variants of concern and SARS-CoV-2 Spike protein-induced syncytia formation. Furthermore,
89 when administered in combination with the antiviral remdesivir (RDV), an intravenous drug that
90 directly targets viral replication via inhibition of the RNA-dependent RNA polymerase (RdRp)
91 (Pruijssers et al., 2020), NTZ synergistically inhibits SARS-CoV-2 growth.

92 Importantly, our study validates the potential of NTZ as a repurposed HDT against COVID-
93 19 in the Syrian hamster infection model. As compared to vehicle-treated infected hamsters, oral
94 administration of NTZ twice-daily resulted in a significant decrease in SARS-CoV-2 morbidity as
95 characterized by both decreased weight loss and lung pathology with dramatic reduction of
96 SARS-CoV-2 viral spike dissemination and syncytia formation. Altogether, these results provide
97 impetus to test and optimize an NTZ-based therapy especially in combination with other promising
98 orally bioavailable antiviral drugs that directly target viral replication.

99 **Results**

100

101 **NTZ and TIZ inhibit SARS-CoV-2 infection in Vero E6 cells in a dose-dependent manner**

102 To determine whether NTZ and its active metabolite TIZ inhibit SARS-CoV-2 replication,
103 we first performed antiviral assays in Vero E6 cells, which are well known to support productive
104 infection with SARS-CoV-2 (Matsuyama et al., 2020) (Suppl. Fig. 1A). Vero E6 cells were thus
105 exposed to increasing concentrations of NTZ, TIZ, or vehicle (DMSO) for 4 hrs before infection
106 with SARS-CoV-2 (isolate USA-WA1/2020) at MOI of 0.025 (see schema in Fig. 1A), and as a
107 positive control, cells were treated in parallel with different concentrations of the RdRp inhibitor
108 RDV. After 48 hrs, the percent of infection across the different conditions was determined by
109 immunostaining for the viral nucleoprotein (N) using a Celigo (Nexcelcom) imaging cytometer and
110 was used to calculate the 50% inhibitory concentration (IC₅₀) of NTZ as previously described
111 (Alwan et al., 1988). The cytotoxicity of NTZ, TIZ, and RDV was evaluated by performing MTT
112 assays on uninfected cells treated with the same compound dilutions in parallel with the antiviral
113 assay. We found that NTZ and TIZ possess strong antiviral activity against SARS-CoV-2 in Vero
114 E6 cells, with IC₅₀s of 4.04 μM and 3.62 μM, respectively, without exhibiting cytotoxicity (Fig. 1B).

115 Using a NeonGreen (NG) expressing SARS-CoV-2 (USA-WA1/2020) recombinant virus
116 (NG-SARS-CoV-2) (Xie et al., 2020), the effect of NTZ on SARS-CoV-2 replication was next
117 assessed by FACS and by imaging flow cytometry using the ImageStream platform (Doan et al.,
118 2018; Haridas et al., 2017; Ranjbar et al., 2019). Cells were pre-treated with 5 or 10 μM NTZ for
119 4 hrs and then infected with NG-SARS-CoV-2 at two different MOIs (0.025 and 0.25) for 48 hrs.
120 In agreement with our findings using the USA-WA1/2020 strain in the antiviral assays above (Fig.
121 1B), we observed dose-dependent NTZ inhibition of the percentage of NG-SARS-CoV-2-infected
122 cells at both MOIs by FACS analysis (Fig. 1C-i).

123 Imaging flow cytometry allows for high-throughput evaluation of SARS-CoV-2 infection at
124 the single cell level (Doan et al., 2018; Haridas et al., 2017; Ranjbar et al., 2019) and quantification
125 of intracellular fluorescence produced by NG-labeled SARS-CoV-2. Using the ImageStream
126 platform, we thus next acquired approximately 3000 cells from vehicle- and NTZ-treated NG-
127 SARS-CoV-2-infected cultures and measured NG fluorescence in each experimental condition.
128 NTZ pre-treatment for 4 hrs prior to SARS-CoV-2 infection resulted in significant inhibition of NG
129 expression at both concentrations of NTZ (5 or 10 μ M) and at both MOIs (0.025 and 0.25)
130 ($p < 0.001$ for each comparison) after 48 hrs (Fig. 1C-ii). We note that representative images of
131 cells that had pixel values at the median level of each condition (marked by the red bar) are
132 displayed showing the NTZ-dependent decreased fluorescence in the infected cells (Fig. 1C-iii).
133 Strikingly, we also observed a significant decrease of the number of infected cells at both NTZ
134 concentrations and both MOIs tested (Fig. 1C-ii) ($p < 0.0001$) for each comparison.

135 Given the robust antiviral activity of NTZ in Vero E6 cells, and based on their different
136 mechanisms of action, we next assessed NTZ's ability to synergize with RDV, which was a
137 standard of care drug treatment to shorten time of COVID-19 recovery (Beigel et al., 2020). To
138 test this hypothesis, we performed combination assays in Vero E6 cells and found that NTZ
139 significantly increases the ability of RDV to inhibit viral infection (Fig. 1D). The results of the
140 combination assay were then further analyzed using SynergyFinder to generate a synergy
141 landscape and combination score by the Loewe model (Fig. 1E) (Ianevski et al., 2020). In this
142 model, a synergistic interaction between drugs is indicated by a score greater than +10, while an
143 additive interaction has a score between -10 and +10, and an antagonistic interaction has a score
144 lower than -10. Notably, the landscape for the interaction of RDV with NTZ shows synergy scores
145 greater than +10 at low NTZ concentrations (6.26 μ M) (Fig. 1E), denoting moderate synergy of
146 the two drugs in the inhibition of SARS-CoV-2 growth. These data are consistent with a study
147 showing that NTZ synergistically enhances the ability of RDV to reduce cytopathic effect (CPE)

148 (Bobrowski et al., 2021). All together, these data show that in Vero E6 cells NTZ robustly inhibits
149 SARS-CoV-2 replication and forms an inhibitory synergistic compound pair with RDV.

150

151 **Validation of NTZ antiviral activity in human cell lines**

152 We next evaluated the ability of NTZ to inhibit SARS-CoV-2 replication in the human cell
153 line A549 transduced with angiotensin-converting enzyme 2 (Ace2). After confirming that the
154 Ace2-A549 cells support SARS-CoV-2 replication (Suppl. Fig. 1B), we pre-treated these cells with
155 increasing concentrations of NTZ, TIZ, RDV, or vehicle (DMSO) for 4 hrs before infection with
156 SARS-CoV-2 (USA-WA1/2020) at an MOI of 0.1. At 48 hrs post-infection, the IC₅₀ and cytotoxicity
157 of each compound was determined as described above. We observed strong antiviral activity of
158 NTZ (IC₅₀ 1.695 μM) and TIZ (IC₅₀ 1.322 μM) against SARS-CoV-2 infection in Ace2-A549 with
159 no cytotoxicity (Fig. 2A). In addition, we also evaluated the effect of NTZ on SARS-CoV-2
160 replication in another human cell line, Ace2-expressing HEK293T cells (Ace2-HEK293T) (Miorin
161 et al., 2020). NTZ similarly inhibited SARS-CoV-2 replication in a dose-dependent manner in
162 Ace2-HEK293T with an IC₅₀ of 2.2 μM (Suppl. Fig. 2).

163 We next pretreated Ace2-A549 cells with 5 or 10 μM NTZ for 4 hrs followed by infection
164 with NG-SARS-CoV-2 (MOI 0.01 and 0.05) for 48 hrs. Analysis by FACS showed that NTZ
165 reduced the percentage of NG-SARS-CoV-2-infected Ace2-A549 cells at both NTZ
166 concentrations and both MOIs (Fig. 2B-i). Furthermore, 5 μM NTZ significantly reduced both the
167 median levels of NG-SARS-CoV2 fluorescence in infected cells and the number of infected cells
168 (Fig. 2B-ii). Images of individual Ace2-A549 cells with pixel numbers that fell at the median level
169 of pixels for the population are displayed in Figure 2B-iii.

170 Interestingly, the IC₅₀ for NTZ in both human cell lines (Ace2-A549: 1.695 μM; Ace2-
171 HEK293T: 2.2 μM) were lower than the IC₅₀ in Vero E6 cells (4.444 μM). Notably, Vero cells are
172 deficient in type I IFN production (Emeny and Morgan, 1979) due to a deletion on chromosome

173 12 resulting in loss of the type I IFN gene cluster (Osada et al., 2014). To interrogate whether
174 signaling through the type I IFN receptor (IFNAR) plays a role in NTZ's ability to inhibit SARS-
175 CoV-2 infection in human cells, we compared NTZ antiviral activity in wild-type and IFNAR knock-
176 out (KO) Ace2-A549 cells. To verify that IFNAR signaling was abrogated in the knock-out cells,
177 we showed that the IFN-dependent phosphorylation of STAT1 and STAT2 (Suppl. Fig. 3A) and
178 transcription of the interferon stimulated gene (ISG) IFITM3 (Suppl. Fig. 3B) were both abolished
179 in the IFNAR-KO Ace2-A549 cells as expected. In addition, we confirmed that Ace2 expression
180 was equivalent in the two cell lines (Suppl. Fig. 3A).

181 The wild-type and IFNAR-KO Ace2-A549 cells were then treated with 10 μ M NTZ or with
182 DMSO for 4 hrs followed by infection with NG-SARS-CoV-2 at an MOI of 0.1 or 0.01 for 48 hrs.
183 Notably, IFNAR-KO Ace2-A549 cells showed a significant increase in the median level of NG
184 fluorescence and also in the numbers of SARS-CoV-2-infected cells at both NTZ concentrations
185 and MOIs tested (Fig. 2C-i). Thus, IFNAR signaling restricts SARS-CoV-2 growth and infection in
186 Ace2-A549 cells. Interestingly, NTZ significantly inhibited both the level of intracellular NG-SARS-
187 CoV-2 fluorescence and the number of infected cells in both WT and IFNAR-KO Ace2-A549 cells,
188 however its ability to inhibit SARS-CoV-2 replication and the number of infected cells was reduced
189 in the IFNAR-KO cells (Fig. 2C-i). Indeed, the median NG fluorescence and the number of infected
190 cells remained significantly higher in the NTZ-treated IFNAR-KO cells compared to the NTZ-
191 treated parental Ace2-A549 cells at both MOIs. Taken together, these results show: (i) IFNAR
192 signaling restricts SARS-CoV-2 replication; (ii) NTZ can inhibit SARS-CoV-2 in the absence of
193 IFNAR signaling; and (iii) IFNAR signaling is required for optimal NTZ inhibition of SARS-CoV-2
194 growth and infection.

195

196 **NTZ inhibits SARS-CoV-2 replication in physiologic human pluripotent stem cell-derived**
197 **cell models**

198 SARS-CoV-2 targets and infects ciliated airway epithelial cells and type 2 pneumocytes in
199 alveolar regions of the lung (Hou et al., 2020). To evaluate the ability of NTZ to restrict SARS-
200 CoV-2 replication in a physiologically relevant cell type, we used two independently derived
201 human pneumocyte *in vitro* models that are generated by the directed differentiation of human
202 pluripotent stem cells (PSCs), the H9 embryonic stem cell line and SPC2-ST-B2 induced
203 pluripotent stem cells (iPSCs) (Hurley et al., 2020). Both H9-derived pneumocyte-like cells (Riva
204 et al., 2020) and the iPSC-derived alveolar epithelial type 2 cells (iAT2s) (Huang et al., 2020)
205 have previously been shown to support SARS-CoV-2 replication. Strikingly, pre-treatment of H9-
206 pneumocytes (Fig. 3A) or iAT2 cells (Fig. 3B) with NTZ for 4 hrs prior to infection with SARS-CoV-
207 2 (isolate USA-WA1/2020) resulted in a significant dose-dependent inhibition of virus replication
208 without significant cytotoxicity. In addition, NTZ's antiviral activity against SARS-CoV-2 in iAT2
209 cells was also validated using the NG-SARS-CoV-2 recombinant virus and the ImageStream
210 platform. We found that NTZ significantly inhibited NG-SARS-CoV-2 fluorescence ($p=0.026$) and
211 the number of NG-SARS-CoV-2 infected cells in the culture ($p<0.0001$) (Fig. 3C). We note that
212 the PSCs from which H9 and iAT2 cells are derived are from two unrelated individuals. Thus, our
213 findings are not specific to an individual and indicate that NTZ inhibits both SARS-CoV-2
214 replication and *de novo* infection of bystander cells in human alveolar epithelial cell cultures that
215 reflect physiological infection.

216

217 **NTZ inhibits virus replication of SARS-CoV-2 variants of concern**

218 Different SARS-CoV-2 variants have contributed to successive waves of the COVID-19
219 epidemic due to their increased transmissibility and virulence, as well as the waning of vaccine-
220 mediated immunity (Harvey et al., 2021). To determine NTZ's activity against three of the recently
221 emerged variants of concern (<https://www.who.int/en/activities/tracking-SARS-CoV-2-variants/>),
222 we treated Vero E6 cells with NTZ for 4 hrs and then infected them with SARS-CoV-2 beta
223 (B.1.351), gamma (P.1), or delta (B.1617.2). As a control, cells were also infected with the original

224 SARS-CoV-2 WA1 strain used in our studies described above. NTZ strongly inhibited the
225 replication of each variant tested similar to its ability to inhibit SARS-CoV-2 WA1 (Fig. 4A). Thus,
226 NTZ is able to inhibit different viral variants with divergent spike proteins that are associated with
227 increased virulence and transmissibility.

228 Intriguingly, high-throughput screening of over 3,000 FDA/EMA-approved drugs recently
229 identified niclosamide, which is structurally similar to NTZ (Stachulski et al., 2021), as an effective
230 inhibitor of spike-induced syncytia formation (Braga et al., 2021). To test the hypothesis that NTZ
231 restricts SARS-CoV-2 dissemination by directly inhibiting spike-mediated fusion, we
232 overexpressed spike protein from SARS-CoV-2 (USA-WA1/2020) and SARS-CoV-2 variants
233 alpha (B.1.1.7), beta (B.1.351), gamma (P.1), and delta (B.1617.2) in Vero-TMPRSS2 cells. Four
234 hours after transfection, 15 μ M NTZ or vehicle (DMSO) was added to the cultures and 24 hrs later
235 cells were fixed to evaluate syncytia formation. NTZ broadly and significantly inhibited syncytia
236 formation induced by overexpression of spike from the USA-WA1/2020 strain and from each
237 variant tested in this assay. Consistent with their increased virulence compared to the USA-
238 WA1/2020 strain, the four variants exhibited significantly higher levels of syncytia formation (Fig.
239 4B), concordant with a recent report (Escalera et al., 2021). These data indicate that NTZ targets
240 a cellular process mediating spike-induced cell-cell fusion that is not significantly affected by the
241 spike mutations in the variants tested.

242

243 **Oral administration of NTZ significantly reduces SARS-CoV-2 replication and disease** 244 **pathogenesis in Syrian hamsters**

245 Given the promising antiviral activity of NTZ *in vitro*, we next evaluated its ability to inhibit
246 SARS-CoV-2 infection and disease *in vivo*. We chose the Syrian hamster model of SARS-CoV-2
247 infection, where animals develop severe pneumonia and clinical outcomes (i.e., peak weight loss
248 around 5 days and complete resolution by 14 days post infection), which are predictable (Chan
249 et al., 2020; Imai et al., 2020; Sia et al., 2020). We used a new extended-release formulation

250 of NTZ (NT-300) currently under phase III evaluation (Rossignol et al., 2021), which reaches
251 peak levels 6-8 hrs after ingestion (Haffizulla et al., 2014).

252 Hamsters were split into 3 groups (12 animals/group): (i) naïve (no infection and no
253 treatment); (ii) infected with SARS-CoV-2 (300pfu) with vehicle (PBS) treatment delivered
254 twice daily (BID) to control for hamster manipulation during oral gavage; (iii) infected with
255 SARS-CoV-2 (300 pfu) and with NTZ (300 mg/kg/day) delivered BID by oral gavage. The first
256 NTZ or vehicle dose was administered 6 hours prior to SARS-CoV-2 infection. The second
257 dose was given 6 hours after infection and then NTZ or vehicle was dosed every 12 hours to
258 complete 5 days of therapy. Daily weights were recorded in the 3 groups from the day of
259 infection up until 14 days post infection (dpi). We found significant protection ($p=0.025$) from
260 weight loss at 5 dpi in the NTZ-treated animals compared to animals who were treated with
261 PBS and observed strong trends of protection at 4 dpi ($p=0.056$) and 6 dpi ($p=0.80$) (Fig. 5A).
262 In addition, animals from each group were sacrificed at 2, 5, and 14 dpi and lungs were
263 collected and processed for viral titer determination and histopathological evaluation. NTZ-
264 treated SARS-CoV-2-infected animals displayed lower viral titers in lung biopsies as
265 compared to mock treated SARS-CoV-2-infected animals ($p=0.057$) at 2 dpi (Fig. 5B).

266 In a complementary approach, we used immunohistochemistry targeting the SARS-CoV-
267 2 Spike protein to visualize and measure the dissemination of infection within the lung. In addition,
268 we quantified the levels of Spike protein expression in the lung by calculating the positive pixels
269 of SARS-CoV-2 Spike immunoreactivity per micron of tissue (Fig. 5C and Suppl. Table 2). As
270 shown in the graph in Fig. 5C, SARS-CoV-2 Spike protein expression was only detected at 2 dpi,
271 irrespective of the cohort, and was significantly less in the NTZ-treated SARS-CoV-2-infected
272 group ($p=0.0496$) as compared to the vehicle-treated SARS-CoV-2-infected cohort. This is
273 consistent with the decline in infectious virus particles we observed at 2 dpi in the NTZ-treated
274 animals (Fig. 5B).

275 While SARS-CoV-2 Spike was mostly located in bronchiole epithelium in both the vehicle-
276 and NTZ-treated infected hamsters at 2 dpi, in the SARS-CoV-2-vehicle treatment group, Spike
277 was more plentiful, with near-complete circumferential involvement of bronchioles that routinely
278 disseminated to smaller distal airways with sporadic involvement of cuboidal pneumocytes
279 interpreted to represent alveolar type 2 pneumocytes, and Spike was evident in the interstitial
280 compartment of the lungs. By contrast, in the NTZ-treated group, almost all the SARS-CoV-2
281 Spike was located in the proximal airways with a more localized and segmental distribution, and
282 it was not detected in the interstitial compartment in lungs from NTZ-treated animals (see
283 magnification of images in Fig. 5C). By 5 dpi, there was minimal residual SARS-CoV-2 Spike
284 observed in both the NTZ- and vehicle-treated SARS-CoV-2-infected groups, which was almost
285 exclusively restricted to sporadic individual bronchiole epithelial cells. No SARS-CoV-2 Spike
286 protein was detected in any cohorts by 14 dpi (data not shown).

287

288 **NTZ improves SARS-CoV-2-driven lung pathology in Syrian hamsters**

289 Lung histopathology was also examined across the 3 experimental cohorts. Individual lung
290 ordinal scores from 1-3 were determined for all animals to quantify severity of infection (Fig. 6B
291 and Suppl. Table 2), and representative lung H&E images are shown (Fig. 6A and Suppl. Fig. 5).
292 At 2 dpi the interstitial score was significantly decreased ($p=0.026$) in the NTZ-treated animals
293 compared to the SARS-CoV-2-infected vehicle-treated animals (Fig. 6B). This was reflected by
294 the absence of, or minimal, lymphohistiocytic and neutrophilic alveolar and/or septal infiltrate in
295 the group of NTZ-treated animals (Fig. 6A). While at 2 dpi the airway score for NTZ- vs. vehicle-
296 treated animals did not reach significance (Fig. 6C), three of the four NTZ-treated animals
297 exhibited absence of discernible bronchiole epithelial pathology like that observed in naïve
298 animals, with a dramatic decline in neutrophilic and histiocytic luminal infiltrate compared to
299 vehicle-treated animals in the one animal that did display airway injury (Fig. 6A). Histologically,
300 this was reflected by less severe and more segmental necrotizing bronchiolitis (see magnified

301 image in Suppl. Fig. 5). Blood vessel scores for NTZ- vs. vehicle-treated animals at 2 dpi also did
302 not reach significance, however again we note that three of the four NTZ-treated animals exhibited
303 an absence of any detectable perivascular infiltrate similar to naïve animals.

304 NTZ therapy was halted at 4 dpi with 5 days of total treatment. At 5 dpi, lung pathology
305 scores were ubiquitously severe, with no clear distinction between the cohorts in any of the
306 anatomical compartments examined (Figs. 6A and 6B). The precise mechanism for the uniform
307 severity observed across the SARS-CoV-2-infected animals +/- NTZ at 5 dpi is unknown. We note
308 that this observation mirrors findings described in an intramuscular DNA vaccine platform
309 encoding SARS-CoV-2 Spike protein, which showed immunologic correlates of protection and a
310 decrease in viral load in Syrian hamsters, but no clear mitigation in lung pathology at 4 dpi
311 compared to positive controls (Leventhal et al., 2021).

312 At 14 dpi, no residual pathology was evident in the airways and the severity of interstitial
313 pathology was minimal to mild in all cohorts (Fig. 6A), which was reflected by small residual
314 clusters of AT2 hyperplasia with minimal histiocytic and neutrophilic infiltrate (Suppl. Fig. 5) with
315 no significant difference in interstitial scores between the groups (Fig. 6B). Notably, blood vessel
316 scores at 14 dpi were significantly decreased ($p=0.012$) in the NTZ-treated group compared to
317 the vehicle-treated group (Fig. 6B), where all four NTZ-treated animals had a clear decrease in
318 residual perivascular lymphohistiocytic infiltrates at 14 dpi compared to vehicle-treated animals
319 (Fig. 6B and Suppl. Fig. 5).

320 We next evaluated H&E lung images to identify potential differences in the levels of SARS-
321 CoV-2-induced syncytia between vehicle- and NTZ-treated hamsters. Strikingly, we observed
322 multiple, often neighboring, syncytial epithelial cells in lungs from all the vehicle-treated SARS-
323 CoV-2-infected animals at 5 dpi (Fig. 6C), which occurred exclusively in areas of bronchiole
324 hyperplasia. By contrast, syncytia formation was rarely observed in the NTZ-treated group, and
325 when observed consisted of a single isolated syncytium within an area of bronchiole hyperplasia
326 (Fig. 6C). Notably, syncytia were not observed at either 2 or 14 dpi in any SARS-CoV-2-infected

327 animals irrespective of treatment group; importantly, syncytia were never observed in naïve
328 animals.

329 **DISCUSSION**

330

331 A critical objective in the global effort to significantly reduce COVID-19 morbidity and
332 mortality is the development of a scalable, well-tolerated, and cost-effective oral therapeutic or
333 cocktail that can be deployed in resource-limited settings as well as in the global north. Here, we
334 provide *in vitro* and *in vivo* data in physiological models of infection showing that NTZ significantly
335 restricts the replication of different SARS-CoV-2 variants of concern *in vitro*, and inhibits virus-
336 induced morbidity, inflammation, and viral dissemination *in vivo* in the Syrian hamster model.
337 Together, these studies suggest that NTZ could have a potential role as an oral therapeutic in the
338 treatment of COVID-19 and its long-term complications or as a prophylactic in high-risk
339 exposures.

340 Multiple host processes have been implicated in the ability of NTZ to inhibit viral
341 replication. In this respect, we previously showed that NTZ inhibition of EBOV replication is
342 significantly impaired in cells deficient in the RNA sensors PKR and RIG-I (Jasenosky et al.,
343 2019). EBOV viral protein 35 (VP35), a protein produced early in infection, binds to dsRNA
344 replicative intermediates shielding EBOV from cytoplasmic sensors including RIG-I and PKR
345 (Cardenas et al., 2006; Feng et al., 2007; Leung et al., 2009; Leung et al., 2010; Schumann et
346 al., 2009), and a second EBOV protein, viral protein 24 (VP24), blocks the activation and nuclear
347 accumulation of STAT1 and inhibits IFN-responsive gene transcription (Reid et al., 2006; Reid et
348 al., 2007; Xu et al., 2014; Zhang et al., 2012). Thus, NTZ, at least in part, overrides EBOV
349 mechanisms of viral innate immune evasion via its ability to amplify PKR- and RIG-I-dependent
350 RNA sensing (Jasenosky et al., 2019). By contrast, the ability of NTZ to inhibit VSV infection is
351 impaired in GADD34- and RIG-I-deficient cells, but not in PKR-deficient cells (Jasenosky et al.,
352 2019). Thus, NTZ has the ability to inhibit viral replication by broadly amplifying RNA sensing
353 pathways, but the specific host factors mediating its antiviral activity may differ during infection
354 with different viruses (Jasenosky et al., 2019).

355 Here, we find that the antiviral activity of NTZ is enhanced by functional type-I IFN
356 signaling. However, in the context of SARS-CoV-2 infection, NTZ was still able to significantly
357 inhibit viral replication in type-I IFN-deficient Vero E6 cells and IFNAR-KO Ace2-A549 cells. It will
358 be important in the future to assess whether the induction of type III IFN genes and the expression
359 of a specific set of IFN-independent ISGs are contributing to this residual NTZ activity. Recent
360 studies have shown that MDA5 and LGP2 are the major pattern recognition receptors involved in
361 SARS-CoV-2 restriction (Sampaio et al., 2021; Yin et al., 2021). We previously showed that NTZ
362 enhances the transcription and the signaling activity of MDA5 (Jasenosky et al., 2019; Ranjbar et
363 al., 2019). However, the role of the MDA5-LGP2 sensing pathway in the antiviral activity of NTZ
364 during SARS-CoV-2 infection remains to be defined and is currently a subject of investigation.

365 Interestingly, NTZ was previously shown to effectively inhibit the replication of influenza
366 and parainfluenza viruses *in vitro* by impairing maturation and intracellular trafficking of their
367 fusion glycoproteins (Piacentini et al., 2018; Rossignol et al., 2009). Furthermore, NTZ and
368 niclosamide interact with TMEM family members TMEM16A and 16F, which are calcium-activated
369 ion channels and lipid scramblases responsible for the exposure of phosphatidylserine on the cell
370 surface (Braga et al., 2021; Caputo et al., 2008; Schroeder et al., 2008; Yang et al., 2008). Both
371 drugs can function as TMEM16A antagonists, which attenuate bronchoconstriction (Miner et al.,
372 2019). Moreover, niclosamide inhibits SARS-CoV-2 Spike-driven syncytia formation by
373 antagonizing the activity of TMEM16F (Braga et al., 2021). Our results showing that NTZ broadly
374 inhibits syncytia formation driven by SARS-CoV-2 Spike from major variants of concern are
375 consistent with these studies and further broaden NTZ's mechanism of action in viral infection.
376 This finding is also consistent with the significant reduction of the number of SARS-CoV-2-infected
377 cells in NTZ-treated cultures, and with the ability of NTZ to synergize with RDV given their
378 independent mechanisms of action. It remains to be demonstrated whether or not NTZ alters
379 spike maturation and intracellular trafficking, or if NTZ regulates the activity of members of the
380 TMEM16 family in the context of infection.

381 Strikingly, oral administration of NTZ to SARS-CoV-2-infected Syrian hamsters results in
382 a significant reduction of virus-induced weight loss and lung viral load. Consistently, NTZ
383 treatment clearly affected Spike expression levels and distribution patterns within the lungs from
384 infected hamsters. Furthermore, animals that had been treated with NTZ also exhibited a
385 reduction of viral syncytial cells in their lungs. Whether this is directly due to the ability of NTZ to
386 inhibit syncytia formation or is a consequence of the decreased viral load and spike expression is
387 not yet known. Importantly, in addition to the significant decrease in spike dissemination, we also
388 observed a dramatic decrease in bronchiolar epithelial degeneration/necrosis with reduced
389 recruitment of inflammatory cells to bronchiolar lumina and lung interstitia at 2 dpi and to
390 perivascular compartments at 14 dpi when hamsters who received NTZ recovered from infection.
391 These results suggest that NTZ may inhibit injury to permissive cell types and ameliorate
392 subsequent recruitment of inflammatory cells that could cause inflammatory complications of
393 SARS-CoV-2 infection.

394 Intriguingly, an initial trial of NTZ treatment in patients (n=50) with moderate COVID-19
395 disease showed that 5 days of treatment was associated with decreased inflammatory
396 biomarkers, faster SARS-CoV-2 PCR negativity, and decreased time to hospital discharge (Blum
397 et al., 2021). Furthermore, a randomized controlled trial (RCT) (n=379) of 5 days of placebo or
398 NTZ treatment for mild or moderate COVID-19 using the extended-release formulation of NTZ
399 (NT-300) was associated with an 85% reduction in progression to severe illness (Rossignol et al.,
400 2021). In both trials NTZ was well tolerated and there were no major adverse events. Here, our
401 *in vivo* studies in the hamster model demonstrating that NTZ significantly reduces morbidity,
402 inflammation, and viral dissemination are consistent with these studies.

403 Moreover, our demonstration that NTZ significantly inhibits SARS-CoV-2 growth,
404 synergizes with RDV, and significantly inhibits different SARS-CoV-2 variants of concern including
405 the more pathogenic delta (B.1617.2) variant, suggests that combining NTZ with another orally
406 available antiviral could form a promising cocktail to treat SARS-CoV-2 infection. In this case,

407 addition of NTZ to new oral antivirals shown to reduce hospitalization and death, such as
408 molnupiravir or Paxlovid (Jayk Bernal et al., 2021; Ledford, 2021), or with intravenously delivered
409 RDV, which has recently been shown to significantly decrease progression of disease in
410 individuals at high risk (Gottlieb et al., 2021), could potentially mitigate viral spread in organs,
411 inflammatory complications, and disease in high-risk exposures including immunosuppressed
412 individuals where viremia is persistent and difficult to treat.

413 Finally, NTZ has a long safety profile in adults and children, has a pediatric syrup
414 formulation, and is well-tolerated in HIV-infected individuals (Rosignol, 2014; Wang et al., 2020).
415 An NTZ-based combination cocktail based on synergy could therefore potentially lower the
416 dosage requirement of expensive and scarce new antiviral oral drugs that have a shorter history
417 of safety data; this could be especially helpful in treatment of children and in immunosuppressed
418 HIV-infected individuals. Furthermore, the oral formulation, inexpensive cost, and wide global use
419 of NTZ make it easily deployable and accessible in resource-constrained settings.

420 MATERIALS AND METHODS

421

422 Cell lines

423 Vero E6 (ATCC, CRL-1586), A549 (ATCC, CRM-CCL-185)-derived, and HEK293T
424 (ATCC, CRL-3216)-derived cell lines were maintained in DMEM (Corning) supplemented with
425 10% FBS (Peak Serum) and Penicillin/Streptomycin (Corning) at 37°C and 5% CO₂. hACE2-
426 A549 cells used in Fig. 2A (Daniloski et al., 2021) and hAce2-HEK293T (Miorin et al., 2020) were
427 previously described. Vero TMPRSS2 (BPS Bioscience, 78081) cells were maintained in DMEM
428 (Corning) supplemented with 10% FBS (Peak Serum), non-essential amino acids, sodium
429 pyruvate (Corning), Penicillin/Streptomycin (Corning), and puromycin (3 µg/mL) (InvivoGen).
430 IFNAR KO A549 cells were generated by CRISPR-Cas9 ribonucleoprotein (RNP) complex (IDT)
431 transfection using the Nucleofector system (Lonza Bioscience). Specifically, a predesigned Alt-R
432 CRISPR-Cas9 gRNA targeting exon 1 (design ID: Hs.Cas9.IFNAR1.1.AK), the ATTO 550 Alt-R
433 CRISPR-Cas9 tracrRNA, and the Alt-R S.p. HiFi Cas9 Nuclease were used to form CRISPR-
434 RNPs *in vitro*. Wild type and IFNAR KO A549 cells were then transduced with an Ace2 expression
435 vector simultaneously using a pTRIP-SFFV-Blast-2A-myc-hACE2 construct, a kind gift from Nir
436 Hacohen and Matteo Gentili (Massachusetts General Hospital and the Broad Institute),
437 sequenced, and then functionally validated (Suppl. Fig. 3). All cell lines used in this study were
438 regularly screened for mycoplasma contamination using the Universal Mycoplasma Detection Kit
439 (ATCC, 30-1012K).

440

441 Viruses

442 SARS-CoV-2 isolate USA-WA1/2020 (BEI Resources NR-52281) stocks were grown in
443 Vero E6 cells as previously described (Miorin et al., 2020). hCoV-19/Japan/TY7-503/2021 (P.1)
444 was obtained from BEI Resources (NR-54982). hCoV-19/USA/MD-HP01542/2021 JHU (B.1.351)
445 was a kind gift from Dr. Andy Pekosz. The SARS-CoV-2 Delta variant (B.1.617.2 PV29995) was

446 obtained from Dr. Viviana Simon (Mount Sinai Pathogen Surveillance Program). B.1.351,
447 B.1.617.2, and P.1 viral stocks were grown on Vero TMPRSS2 cells. All viruses were validated
448 by genome sequencing. NG-SARS-CoV-2, a stable monomeric NeonGreen-labeled SARS-CoV-
449 2 virus (icSARS-CoV-2-mNG), was a kind gift from Pei-Yong Shi (University of Texas Medical
450 Branch) (Xie et al., 2020). Virus was reconstituted from lyophilized sample and then titered using
451 Vero cells as described (Huang et al., 2020; Xie et al., 2020). All experiments performed with a
452 SARS-CoV-2 isolate were performed in accordance with biosafety protocols developed by
453 ISMMS, the Ragon Institute of MGH, MIT and Harvard, or the National Emerging Infectious
454 Diseases Laboratories of Boston University.

455

456 ***In vitro* antiviral growth assay**

457 Vero E6, Ace2-A549, or Ace2-HEK293T cells were seeded in 96-well plates in DMEM
458 (10% FBS) and incubated for 24 h at 37°C and 5% CO₂. Four hours before infection the medium
459 was replaced with 100 µl of DMEM (2% FBS) containing the compound of interest (NTZ, TIZ, or
460 remdesivir) at concentrations 50% greater than those indicated, including a DMSO control. Plates
461 were then transferred into the BSL-3 facility and infected at the desired MOI in 50 µl of DMEM
462 (2% FBS), bringing the final compound concentration to those indicated. Plates were then
463 incubated for 48 h at 37°C. After infection, supernatants were removed, and cells were fixed with
464 4% paraformaldehyde for 24 hours prior to being removed from the BSL-3 facility. The cells were
465 then immunostained for the viral NP protein (an in-house mAb 1C7 provided by Dr. Thomas
466 Moran, Mount Sinai School of Medicine) with a DAPI counterstain. Infected cells (488 nm) and
467 total cells (DAPI) were quantified using a Celigo (Nexcelcom) imaging cytometer. Percent
468 infection was quantified as ([infected cells/total cells]-background) multiplied by 100 and the
469 DMSO control was set to 100% infection for analysis. The IC₅₀ was determined using GraphPad
470 Prism software. Cytotoxicity was performed using the MTT assay (Roche) in uninfected cells with
471 the same compound dilutions and concurrent with the viral replication assay. All assays were

472 performed in biologically independent triplicates. Remdesivir was purchased from Medkoo
473 Biosciences, Inc.

474

475 ***In vitro* viral growth and infection analysis by FACS and Imaging Flow Cytometry**

476 For standard flow-cytometric analyses, cells treated with NTZ or mock treated and infected
477 with NG-SARS-CoV2 and were terminated at the indicated time points. Cells were washed with
478 PBS, fixed with 4% paraformaldehyde for 24 hrs and acquired on a BD FACSCanto. NeonGreen
479 fluorescent infected cells were evaluated using Flow-Jo software after gating on live cell
480 populations. For ImageStream analysis, cells treated with NTZ or mock treated and infected with
481 NG-SARS-CoV2 were terminated at the indicated time points. Cells were washed with PBS and
482 fixed with 4% paraformaldehyde for 24 hrs. Next, 3000 gated cells were acquired on an Amnis
483 ImageStream^x Mark II imaging flow cytometer (EMD Millipore). Live focused single cells were
484 gated and NeonGreen fluorescent positive cells were evaluated using Ideas software and pixels
485 were exported for further analysis on Prism to graph the dot plots and compare NTZ-treated to
486 mock by the Mann-Whitney two-tailed test. To compare the numbers of NTZ-treated infected cells
487 to mock-treated cells we used the Fisher exact test using Stata 12 software.

488

489 **H9 stem cell-derived pneumocyte-like cell differentiation and SARS-CoV-2 infection**

490 Human embryonic stem cells (H9, WiCell, WA09) were cultured with mTeSR (STEMCELL
491 Technologies, 85850) on Vitronectin XF (STEMCELL Technologies, 07180)-coated tissue culture
492 plates and split in a ratio of 1:6 to 1:12 every four to six days with Gentle Cell Dissociation Reagent
493 (STEMCELL Technologies, 07174). Alveolar differentiation was induced as previously described
494 (Riva et al., 2020; White et al., 2021). Viral infections were performed in the BSL-3 facility on day
495 nine after induction of differentiation, in accordance with biosafety protocols developed by ISMMS.
496 Cells were fixed and analyzed two days post-infection. For assessment of infection rates, H9 cells
497 were washed once with PBS, detached with 5 mM EDTA for 5 min at 37°C, and then fixed with

498 4% paraformaldehyde. Cells were washed in PBS supplemented with 2 mM EDTA, permeabilized
499 using Perm/Wash buffer (BD Biosciences), and subsequently stained for 1 h at room temperature
500 with anti-NP mAb 1C7 antibody labeled with an Alexa488-fluorescent marker using the Alexa
501 Fluor™ 488 Antibody Labeling Kit (Invitrogen). Immunofluorescence-labelled cells were washed
502 twice in PBS-EDTA after incubation with the antibody and then subjected to flow-cytometry
503 analysis using a Gallios flow cytometer (Beckman Coulter). Cytotoxicity of the compounds was
504 assessed using the MTT assay (Roche) in uninfected cells treated with the same compound
505 dilution and concurrent with the viral replication assay.

506

507 **iPSC differentiation into alveolar epithelial type 2 cells (iAT2s) for air-liquid interface** 508 **culture and SARS-CoV-2 infection**

509 Previously published human iPSCs (Huang et al., 2020) carrying an SPC2-SFTPC^{tdTomato}
510 reporter (iPSC clone SPC2-ST-B2, Boston University (Hurley et al., 2020)) were differentiated
511 into alveolar epithelial type 2 cells (iAT2s) and maintained as alveolospheres embedded in three-
512 dimensional (3D) Matrigel in “CK+DCI” media, as previously described (Jacob et al., 2019). iAT2s
513 were serially passaged approximately every 2 weeks by dissociation into single cells via the
514 sequential application of dispase (2 mg/mL; Thermo Fisher Scientific; 17105-04) and 0.05%
515 trypsin (Invitrogen; 25300054) and replated at a density of 400 cells/ μ L of Matrigel (Corning;
516 356231), as previously described (Jacob et al., 2019). To generate air-liquid interface (ALI)
517 cultures, iAT2s were seeded at 520,000 live cells/cm² on Transwell inserts (Corning Cat#3470),
518 and apical media was removed 2 days post-seeding. After 7 days post-seeding, iAT2 ALI cultures
519 were ready to be infected with SARS-CoV-2 USA_WA1/2020 or SARS-CoV-2-mNG at an MOI of
520 0.04, along with mock controls. Prior to infection, RDV (Selleck Chem Cat#S8932) or NTZ was
521 added to the apical and basolateral sides of the Transwell inserts for 30 minutes as indicated.
522 The apical side was subsequently aspirated and replaced by SARS-CoV-2 diluted in CK+DCI
523 media for one hour. At 2 days post-infection, samples were collected for downstream processing.

524 For flow cytometry and trypan blue staining, 200 μ L of Accutase (Sigma Cat# A6964) was added
525 apically and incubated for 20 minutes at room temperature. The cells were collected and used
526 directly for trypan blue staining or fixed with 10% formalin for at least 6 hours at 4°C and
527 subsequently removed from BSL-4 prior to FACS analysis. After single cell suspension, analysis
528 was performed by immunostaining for the viral NP protein as described for the H9-pneumocytes
529 or by imaging flow cytometry using the ImageStream platform. For fluorescence microscopy, iAT2
530 ALI cultures were fixed with 10% formalin for at least 6 hours at 4°C at the indicated times post-
531 infection. Samples were then removed from BSL-4 and washed with PBS three times for 5
532 minutes at room temperature. Cell nuclei on the transwell inserts were stained with DAPI dye
533 (1:500, Life Technologies). The Transwell insert membranes were then cut out and mounted on
534 slides using ProLong Diamond Antifade Mountant (Invitrogen Cat#P36965). Slides were imaged
535 on a confocal microscope (Leica SP5).

536

537 **Antiviral combination assay**

538 2,000 Vero E6 cells per well were seeded into 96-well plates in DMEM (10% FBS) and
539 incubated for 24 h at 37°C and 5% CO₂. Two hours before infection, the medium was replaced
540 with 100 μ l of DMEM (2% FBS) containing the combination of NTZ and RDV following a dilution
541 combination matrix. A 6 by 6 matrix of drug combinations was prepared in triplicate by making
542 serial two-fold dilutions of the drugs on each axis, including a DMSO control column and row. The
543 resulting matrix had no drug in the right upper well, a single drug in rising 2-fold concentrations in
544 the vertical and horizontal axes starting from that well, and the remaining wells with rising
545 concentrations of drug mixtures reaching maximum concentrations of the drugs at the lower left
546 well. Plates were then transferred into the BSL-3 facility and SARS-CoV-2 (MOI 0.025) was added
547 in 50 μ l of DMEM (2% FBS), bringing the final compound concentration to those indicated in the
548 figures. Plates were then incubated for 48 h at 37°C. After infection, cells were fixed with
549 formaldehyde for 24 hours prior to being removed from the BSL-3 facility. The cells were then

550 immunostained for the viral NP protein as described above. This combination data was analyzed
551 using SynergyFinder (Ianevski et al., 2020) by the Loewe method (Loewe, 1953).

552

553 **Spike-induced syncytia assay**

554 30,000 Vero-TMPRSS2 cells were reverse transfected with 100 ng of pCAGGS-S
555 plasmids in a black 96-wellplate using TransIT-LT1 Transfection reagent (Mirus) in complete
556 growth medium (containing 10% FBS). 4 hrs after transfection, medium containing transfection
557 complexes was removed and replaced by medium containing 2% FBS and either DMSO or 15
558 μ M NTZ. Cells were incubated for 24 hrs at 37°C to allow syncytium formation. After 24 h, cells
559 were fixed with 4% paraformaldehyde in PBS (15 min), permeabilized with 0.1% Triton X-100
560 (15 min) and stained for 30 min with 2 μ g/ml HCS Cell Mask stain (Life Technologies). Syncytia
561 were counted microscopically in triplicate wells. The pCAGGS-S plasmids used in this assay have
562 been previously described (Escalera et al., 2021).

563

564 ***In vivo* Syrian hamster infection with SARS-CoV-2**

565 Syrian Golden hamsters 10-12 weeks old (Envigo RMS, LLC), n = 42, were divided into 3
566 groups of 14: naïve (n = 14), SARS-CoV-2-infected mock (PBS) treatment cohort (n = 14), and
567 SARS-CoV-2-infected NTZ (NT-300, a gift from Romark, Inc)-treated at 300 mg/kg/per day bi-
568 daily cohort (n = 14). Hamsters in the infected cohorts were infected intranasally with SARS-CoV-
569 2 (isolate USA-WA1/2020) in a 50 μ l suspension containing a targeted dose of 100 PFU (actual
570 dose was 300 PFU). On the day of SARS-CoV-2 challenge the mock cohort was treated with
571 sterile PBS and the NTZ-treated cohort was treated with 150 mg/kg of NTZ at 6 hours before
572 challenge and then 6 hours after challenge with subsequent treatments for these 2 cohorts every
573 12 hours (bi-daily) for the remaining 4 days of treatment. Cohorts were treated via oral gavage
574 using an 18 gauge x 2 inch curved animal feeding needle to deliver 1 ml of volume per treatment.
575 Lungs and sera were harvested for virus load analysis from 4 hamsters per group on day 2, 5,

576 and 14 post SARS-CoV-2 challenge. Weight loss was monitored from the first treatment time
577 point through end of the study on day 14 post SARS-CoV-2 challenge. Weight loss was monitored
578 for all hamsters throughout the study for humane endpoint criteria. Percent weight loss data (Fig.
579 4A) were derived from 6 hamsters that went to study endpoint at day 14 post-SARS-CoV-2
580 challenge.

581

582 **Plaque assay**

583 Plaque assays were performed using Vero E6 cells as previously described (Amanat et
584 al., 2020). Briefly, Vero E6 cells seeded in 12-well plate format were infected with serial ten-fold
585 dilutions of supernatants from homogenized lung tissues. Virus absorption was carried out for 1
586 hour using an inoculum of 200 μ l and rocking the plates every 10-15 min. After 1 hour, the
587 inoculum was removed, and the cells were incubated with an overlay composed of MEM with 2%
588 FBS and 0.7% Oxoid agar for 72 hours at 37°C with 5% CO₂. The plates were subsequently fixed
589 using 5% formaldehyde and immuno-stained using a monoclonal anti-SARS-CoV-NP antibody
590 (Creative-Biolabs; NP1C7C7). In brief, plates were blocked (3% skim-milk TBS with 0.1%
591 Tween20 for 1 h), stained for 90 min with anti-NP antibody (mAb 1C7, diluted 1:1000 in 1% skim-
592 milk TBS with 0.1% Tween20), and finally secondary-stained with anti-mouse-HRP (antibody
593 diluted 1:5000 in 1% skim-milk TBS with 0.1% Tween20 for 45 mins). Plates were incubated for
594 10 min with KPL TrueBlue peroxidase substrate (Seracare) to reveal staining.

595

596 **Pathology analysis: histologic processing and semi-quantitative analysis**

597 Tissue samples were fixed for a minimum of 7 days in 10% neutralized buffered formalin
598 before being removed from BSL-4 and subsequently processed in a Tissue-Tek VIP-6 automated
599 vacuum infiltration processor (Sakura Finetek) and embedded in paraffin using a HistoCore
600 Arcadia paraffin embedding machine (Leica). 5 μ m tissue sections were generated using an
601 RM2255 rotary microtome (Leica) and transferred to positively charged slides, deparaffinized in

602 xylene, and dehydrated in graded ethanol. Tissue sections were stained with hematoxylin and
603 eosin for histologic examination, with additional serial sections utilized for immunohistochemistry
604 (IHC). A Ventana Discovery Ultra (Roche) tissue autostainer was used for IHC. Specific protocol
605 details are outlined in Suppl. Table 1. In brief, SARS-CoV-2 spike protein monoplex IHC was
606 conducted using a Chromomab DAB IHC kit (Roche, Basel, Switzerland) with CC1 antigen
607 retrieval at 95°C for 64 minutes, primary incubation at 1:900 for 40 min at room temperature,
608 rabbit anti-IgG1+IgG2a+IgG3 antibody (ab133469) at 37°C for 20 minutes (1:1,000), and
609 ImmPRESS HRP Goat Anti-Rabbit IgG polymer pre-dilute detection (Vector Laboratories) at 37°C
610 for 20 minutes. Uninfected animals served as negative controls, while SARS-CoV-2 animals
611 receiving PBS and no therapeutic served as positive controls confirming the specificity of the
612 assay. Histomorphological analysis was performed by a single board-certified veterinary
613 pathologist (N.A.C.), who developed an ordinal grading score encompassing the diversity and
614 severity of histologic findings outlined in Table 2. Histologic criteria were broken down into three
615 compartments: airways, blood vessels, and interstitium, with results utilized to generate a
616 cumulative lung injury score. This score also incorporated the overall degree of immunoreactivity
617 to the SARS-CoV-2 Spike antigen. A summary of individual animal scores and specific criteria
618 utilized to score lungs is included in Suppl. Tables 1 and 2.

619

620 **Quantitative Image Analysis**

621 Digitized whole slide scans were analyzed using the image analysis software HALO
622 (Indica Labs, Inc., Corrales, NM). Slides were manually annotated to select pulmonary
623 parenchyma, excluding non-pulmonary tissues (i.e., tracheobronchial lymph nodes, adipose
624 tissue, etc.). Quantitative outputs were obtained using the Area Quantification (AQ) module, which
625 reports total area of immunoreactivity of a specified parameter within a region of interest. Values
626 are given as a percentage of total tissue area analyzed. Minimum dye intensity thresholds were

627 established using the real-time tuning field of view module to accurately detect positive

628 immunoreactivity for SARS-CoV-2 Spike antigen.

629

630 **ACKNOWLEDGEMENTS**

631

632 This work was funded by grants from the Annenberg Foundation, Fast Grants, and the
633 NIH (R21AI151732), and a laboratory gift from Jeanne Sullivan to AEG. This research was also
634 partly funded by grants from CRIPT (Center for Research on Influenza Pathogenesis and
635 Transmission), an NIAID-funded Center of Excellence for Influenza Research and Response
636 (CEIRR, contract 75N93021C00014), NCI SeroNet grant U54CA260560; NIAID grants
637 U19AI135972 and U19AI142733, DARPA grant HR0011-19-2-0020; a supplement to DoD grant
638 W81XWH-20-1-0270, JPB Foundation, Open Philanthropy Project (research grant 2020-215611
639 (5384)), and by anonymous donors to AG-S; and by PRIME (Program for Research on Immune
640 Modeling and Experimentation), an NIAID-funded Modeling Immunity for Biodefense Center
641 (grant U19 AI117873), and CRIP (Center for Research on Influenza Pathogenesis), and an NIAID-
642 funded Center of Excellence for Influenza Research and Surveillance (CEIRS, contract
643 HHSN272201400008C) to AF-S and AG-S. The work was also supported by grants from the NIH
644 (R01HL095993, U01TR001810, N01 75N92020C00005) and Evergrande COVID-19 Response
645 Fund Awards from the Massachusetts Consortium on Pathogen Readiness (MassCPR) to DNK;
646 Fast Grants, NIH (NCATS, UL1TR001430), and MassCPR to EM; MassCPR to RC; SIG grants
647 S10-OD026983 and S10-OD030269 to NAC; NIH (F30HL147426) to KMA; CJ Martin Early
648 Career Fellowship from the Australian National Health and Medical Research Council to RBW;
649 and NIH (U01TR001810, UL1TR001430, R01DK101501, and R01DK117940) to AAW.

650 We thank Romark Inc. for the gift of NTZ-300, S-Y Pei and UTMB for the gift of NG-SARS-
651 CoV-2, Nir Hacohen and Matteo Gentili for the gift of pTRIP-SFFV-Blast-2A-myc-hACE2, and
652 Michael Farzan and Huihui Mu for the gift of pQCXIP-myc-hACE2-c9. We also thank Randy
653 Albrecht for support with the BSL-3 facility and procedures at the ISMMS, Julie Boucou and Xie
654 Yong for support and advice at the BSL-3 facility at the Ragon Institute of MGH, MIT and Harvard,
655 Richard Cadagan, Hans P. Gertje, and Paige Montanaro for technical assistance, and the

656 Microscopy Shared Resource Facility at the Icahn School of Medicine at Mount Sinai. We are
657 grateful to Gail Cassell for helpful discussions through the years.

658 Finally, we are indebted to Wallis Annenberg, Jeanne Sullivan, and the founders of Fast
659 Grants for their critical and early support.

660

661 **Conflict of interest**

662 The AG-S laboratory has received research support from Pfizer, Senhwa Biosciences,
663 Kenall Manufacturing, Avimex, Johnson & Johnson, Dynavax, 7Hills Pharma, Pharmamar,
664 ImmunityBio, Accurius, Nanocomposix, Hexamer, N-fold LLC, Model Medicines, Atea Pharma,
665 and Merck outside of the reported work. AG-S has consulting agreements for the following
666 companies involving cash and/or stock outside of the reported work: Vivaldi Biosciences,
667 Contrafect, 7Hills Pharma, Avimex, Vaxalto, Pagoda, Accurius, Esperovax, Farmak, Applied
668 Biological Laboratories, Pharmamar, Paratus, CureLab Oncology, CureLab Veterinary, and
669 Pfizer. AG-S is inventor on patents and patent applications on the use of antivirals and vaccines
670 for the treatment and prevention of virus infections and cancer, owned by the Icahn School of
671 Medicine at Mount Sinai, New York, outside of the reported work. J-FR is an employee of, and
672 owns an equity interest in, Romark, L.C. The authors claim no other competing interests.

673 **FIGURE LEGENDS**

674

675 **Fig. 1 SARS-CoV-2 replication is inhibited by NTZ or TIZ in Vero E6 cells.**

676 **A.** Schema of the antiviral assay. **B.** Percent inhibition of SARS-CoV-2 replication and cytotoxicity
677 assay in Vero E6 cells in the presence of the indicated drugs: NTZ (nitazoxanide), TIZ
678 (tizoxanide), Remdesivir (RDV). Vero E6 cells were infected with 100 PFU (MOI 0.025) of SARS-
679 CoV-2 (isolate USA-WA1/2020) in the presence of increasing concentrations of drug for 48 hrs,
680 after which viral replication was measured by NP immunostaining as described in Materials and
681 Methods. In all panels, viral infectivity is shown as a solid black line and cell toxicity as a dashed
682 red line. Calculated IC_{50} is indicated in the bottom-left corner of each plot. RDV is included as a
683 standard of care control. **C.** Quantitative inhibition of NeonGreen SARS-CoV-2 in Vero E6 cells
684 measured by flow cytometry and quantitative imaging flow cytometry using the ImageStream
685 platform. Vero E6 cells were pretreated with 5 or 10 μ M NTZ or carrier (DMSO) for 4 hrs and then
686 infected with NeonGreen (NG)-SARS-CoV2 at an MOI of 0.025 or 0.25. At 48 hrs post-infection
687 cultures were fixed for 24 hrs before FACS and ImageStream analysis. (i) The percentage of
688 infection as measured by FACS. Experiments were performed at least three independent times.
689 (ii) Dot plot displaying the quantification of NG pixels as a representation of NG-SARS-CoV-2
690 fluorescence in infected cells (among the 3000 cells acquired). Asterisks indicate significant
691 differences in NTZ-treated samples as compared to DMSO control by two-tailed Mann-Whitney
692 test. $**P < 0.001$ for each comparison. The number of infected cells in each experimental condition
693 is shown at the bottom of the panel. We found significant reduction of infected cells in NTZ-treated
694 cultures at both MOIs and both concentrations of NTZ ($***P < 0.0001$ for each comparison) by
695 Fisher exact test using Stata 12 software. Experiments were performed at least three independent
696 times. (iii) Images of representative NeonGreen-SARS-CoV-2 infected cells were selected from
697 the median levels of pixels shown in the analysis in panel (ii). **D.** Antiviral activity curves by RDV

698 in the presence of increasing concentrations of NTZ. **E.** Synergy landscapes and combination
699 scores generated by the Loewe method using SynergyFinder software.

700

701 **Fig. 2 Antiviral activity of NTZ and TIZ in Ace2-A549 cells.**

702 **A.** Percent inhibition of SARS-CoV-2 replication and cytotoxicity assay in Ace2-A549 cells in the
703 presence of NTZ, TIZ, or RDV. Cells were treated with the indicated drug for 4 hrs prior to infection
704 with SARS-CoV-2 (isolate USA-WA1/2020) at MOI 0.1 for 48 hrs. Viral replication was measured
705 by NP immunostaining as described in Materials and Methods. In all panels, viral infectivity is
706 shown as a solid black line and cell toxicity as a dashed red line. Calculated IC₅₀ is indicated at
707 the bottom of each plot. RDV is included as a standard of care control. **B.** Quantitative inhibition
708 of NG-SARS-CoV-2 in Ace2-A549 cells measured by flow cytometry and quantitative imaging
709 flow cytometry using the ImageStream platform. Ace2-A549 cells were pretreated with 5 or 10 μM
710 NTZ or carrier (DMSO) for 4 hrs before infection at an MOI of 0.05 or 0.01. At 48 hrs post-infection
711 cells were fixed and evaluated by FACS and by quantitative imaging flow cytometry as described
712 in the legend to Fig. 1. (i) The percentage of infection as measured by FACS. Experiments were
713 performed at least three independent times. (ii) Dot plot displaying the quantification of NG pixels
714 as a representation of NG-SARS-CoV-2 fluorescence in infected cells (among the 3000 cells
715 acquired). Asterisks indicate significant differences as compared to DMSO control by two-tailed
716 Mann-Whitney test: ** $P < 0.005$ and * $P < 0.05$. The number of infected cells in each experimental
717 condition is shown at the bottom of the panel. We found significant reduction of infected cells in
718 NTZ-treated cultures at both MOIs and both concentrations of NTZ (** $P < 0.0001$ for each
719 comparison). Experiments were performed at least three independent times. (iii) Images of
720 representative NeonGreen-SARS-CoV-2 infected cells were selected from the median levels of
721 pixels shown in the analysis in panel (ii). **C.** NTZ's inhibitory effect on NG-SARS-CoV-2 growth in
722 wild-type (WT) and IFNAR-KO Ace2-A549 cells. (i) Plots displaying the quantification of NG pixels
723 as in (B). The number of infected cells in each experimental condition is shown at the bottom of

724 the panel. We found significant reduction of infected cells in NTZ treated cultures at both MOIs
725 and both concentrations of NTZ ($***P<0.0001$ for each comparison) by Fisher exact test using
726 Stata 12 software. Experiments were performed at least three independent times. (ii) Images of
727 representative NeonGreen-SARS-CoV-2 infected cells were selected from the median levels of
728 pixels shown in the analysis in panel. In all panels, asterisks indicate significant differences as
729 compared to DMSO control by two-tailed Mann-Whitney test: $*P<0.05$, $**P<0.005$, $***P<0.0001$.

730

731 **Fig 3. NTZ is highly active against SARS-CoV-2 infection in stem cell-derived human lung**

732 **alveolar epithelial cultures. A.** H9-derived pneumocyte-like cells were infected with SARS-CoV-

733 2 (isolate USA-WA1/2020) at an MOI of 0.1 in the presence of the indicated concentrations of

734 NTZ or vehicle (DMSO). All cells were pretreated for 4 hrs and NTZ or DMSO were maintained in

735 the media throughout the experiment. SARS-CoV-2 infection (NP immunostaining) and cell

736 viability (MTT assay) were measured at 48 hrs. Asterisks indicate statistically significant

737 differences as shown on the graph. **B.** iPSC-derived alveolar epithelial type 2 cells (iAT2s) were

738 infected with SARS-CoV-2 (isolate USA-WA1/2020) at an MOI of 0.5 in the presence of the

739 indicated concentrations of NTZ or vehicle (DMSO) as described in Materials and Methods.

740 Percent infection was measured by NP immunostaining and cell viability by trypan blue exclusion

741 performed on infected and treated cells. Asterisks indicate statistically significant differences as

742 shown on the graph. Experiments were performed at least three independent times. **C.**

743 Quantitative imaging flow cytometry IDEAS analysis of NG-SARS-CoV-2-infected iAT2 in the

744 presence of vehicle (DMSO) or NTZ (15 μ M). 3000 cells were acquired on an ImageStream^X Mark

745 II instrument and evaluated for pixel intensity of NeonGreen (left). The median cellular

746 fluorescence of the NG-SARS-CoV-2-infected iAT2 cells was significantly reduced in the NTZ-

747 treated vs. mock-treated cultures ($p=0.026$). The reduction of the number of infected cells in NTZ-

748 treated cultures was significant ($***P<0.0001$) by Fisher exact test using Stata 12 software.

749 Representative images of intracellular NG levels at the median range marked by the red line in
750 the dot plot (right).

751

752 **Fig 4. NTZ inhibits replication of different SARS-CoV-2 VOCs and strongly reduces spike-**
753 **mediated syncytia formation.**

754 **A.** Vero E6 cells were treated with DMSO or 15 μ M NTZ four hrs before infection with the indicated
755 SARS-CoV-2 isolates at an MOI of 0.025 for 48 hrs. Viral replication was measured by NP
756 immunostaining and quantified using a Celigo imaging cytometer as described in Materials and
757 Methods. **B.** Vero TMPRSS2 cells were reverse transfected with 100 ng of pCAGGS plasmids
758 expressing the spike protein from the SARS-CoV-2 variants of concern indicated in the figure.
759 Four hours after transfection, medium containing transfection complexes was removed and
760 replaced by medium containing 2% FBS and either DMSO or 15 μ M NTZ. After 24 hrs, cells were
761 fixed and stained with HCS Cell Mask stain (Life Technologies). **C.** Quantification of spike-induced
762 syncytia formation from (B). Syncytia were counted microscopically in triplicate wells. In all panels,
763 asterisks indicate statistically significant differences ($***P<0.001$).

764

765 **Fig 5. Oral delivery of NTZ significantly reduces weight loss and decreases lung viral load**
766 **in the Syrian hamster model.**

767 **A.** Percent of starting body weight from the day of challenge (day 0) to 14 days post-infection in
768 naïve and SARS-CoV-2 (isolate USA-WA1/2020)-infected Syrian hamsters treated with NTZ 300
769 mg/kg bi-daily or treated with vehicle by oral gavage. Four animals were euthanized on days 2,
770 5, and 14 for lung removal and serum collection. Day 14 was the study endpoint. Asterisk indicates
771 statistically significant differences by one-tailed unpaired Student's t-test. **B.** SARS-CoV-2 titer in
772 lungs from vehicle- and NTZ-treated animals. The *P* value indicated shows the differences at day
773 2 by one-tailed unpaired Mann-Whitney test. Lungs from 4 animals were included in the IHC
774 analysis for each timepoint except for the 2 dpi timepoint, where there were 3 SARS-CoV-2

775 PBS/vehicle-treated animals. **C.** Representative images of lung tissue collected at 2 dpi and
776 subjected to immunohistochemistry with SARS-CoV-2 Spike-specific antibody. Insets show
777 higher magnification of the lung interstitium, where viral antigen was only observed in the SARS-
778 CoV-2 vehicle-treated animals. Scale bars, 100 μ m. Graph shows quantification of pixels of
779 SARS-CoV-2 Spike protein/micron of Syrian hamster lung tissue. Asterisk indicates statistically
780 significant differences by one-tailed unpaired Student's t-test at day 2.

781

782 **Fig 6. NTZ significantly prevents lung pathology SARS-CoV-2 infected Syrian hamsters.**

783 **A.** Comparison of normal lung (naïve) to pathologic changes induced by SARS-CoV-2 in vehicle-
784 vs. NTZ-treated animals at day 2, 5, and 14 post-infection. Lung pathology at 5 dpi was severe
785 irrespective of treatment group. **B.** NTZ significantly reduced interstitial inflammatory and
786 perivascular scores at 2 and 14 days post-infection. Qualitatively there was decreased bronchiole
787 epithelial injury and associated luminal inflammatory exudate. Lung pathology at 5 dpi was severe
788 irrespective of treatment group. Asterisk indicates statistically significant differences by one-tailed
789 unpaired Student's t-test at day 2 for interstitium and on day 14 for blood vessels. Lungs from 4
790 animals were included in the scoring analysis for each timepoint except for 2 dpi, where there
791 were 3 SARS-CoV-2 PBS/vehicle-treated animals. **C.** Bronchiole syncytial cells were observed
792 exclusively at 5 dpi in SARS-CoV-2-inoculated animals and were more frequently observed in the
793 vehicle treated group. Scale bars: A, 100 μ m; C, 50 μ m.

794 **REFERENCES**

- 795
- 796 Alwan, W.H., Dieppe, P.A., Elson, C.J., and Bradfield, J.W. (1988). Bone resorbing activity in
797 synovial fluids in destructive osteoarthritis and rheumatoid arthritis. *Ann Rheum Dis* 47, 198-
798 205.
- 799
- 800 Amanat, F., White, K.M., Miorin, L., Strohmeier, S., McMahon, M., Meade, P., Liu, W.C.,
801 Albrecht, R.A., Simon, V., Martinez-Sobrido, L., *et al.* (2020). An in vitro microneutralization
802 assay for SARS-CoV-2 serology and drug screening. *Curr Protoc Microbiol* 58, e108.
- 803
- 804 Beigel, J.H., Tomashek, K.M., Dodd, L.E., Mehta, A.K., Zingman, B.S., Kalil, A.C., Hohmann,
805 E., Chu, H.Y., Luetkemeyer, A., Kline, S., *et al.* (2020). Remdesivir for the treatment of Covid-
806 19 - final report. *N Engl J Med* 383, 1813-1826.
- 807
- 808 Blum, V.F., Cimerman, S., Hunter, J.R., Tierno, P., Lacerda, A., Soeiro, A., Cardoso, F., Bellei,
809 N.C., Maricato, J., Mantovani, N., *et al.* (2021). Nitazoxanide superiority to placebo to treat
810 moderate COVID-19 - A Pilot prove of concept randomized double-blind clinical trial.
811 *eClinicalMedicine* 37, 100981.
- 812
- 813 Bobrowski, T., Chen, L., Eastman, R.T., Itkin, Z., Shinn, P., Chen, C.Z., Guo, H., Zheng, W.,
814 Michael, S., Simeonov, A., *et al.* (2021). Synergistic and antagonistic drug combinations against
815 SARS-CoV-2. *Mol Ther* 29, 873-885.
- 816
- 817 Braga, L., Ali, H., Secco, I., Chiavacci, E., Neves, G., Goldhill, D., Penn, R., Jimenez-Guardeno,
818 J.M., Ortega-Prieto, A.M., Bussani, R., *et al.* (2021). Drugs that inhibit TMEM16 proteins block
819 SARS-CoV-2 spike-induced syncytia. *Nature* 594, 88-93.
- 820
- 821 Caputo, A., Caci, E., Ferrera, L., Pedemonte, N., Barsanti, C., Sondo, E., Pfeffer, U., Ravazzolo,
822 R., Zegarra-Moran, O., and Galletta, L.J. (2008). TMEM16A, a membrane protein associated
823 with calcium-dependent chloride channel activity. *Science* 322, 590-594.
- 824
- 825 Cardenas, W.B., Loo, Y.M., Gale, M., Jr., Hartman, A.L., Kimberlin, C.R., Martinez-Sobrido,
826 L., Saphire, E.O., and Basler, C.F. (2006). Ebola virus VP35 protein binds double-stranded RNA
827 and inhibits alpha/beta interferon production induced by RIG-I signaling. *J Virol* 80, 5168-5178.
- 828
- 829 Chan, J.F., Zhang, A.J., Yuan, S., Poon, V.K., Chan, C.C., Lee, A.C., Chan, W.M., Fan, Z., Tsoi,
830 H.W., Wen, L., *et al.* (2020). Simulation of the clinical and pathological manifestations of
831 Coronavirus Disease 2019 (COVID-19) in golden Syrian hamster model: implications for
832 disease pathogenesis and transmissibility. *Clin Infect Dis* 71, 2428-2446.
- 833
- 834 Daniloski, Z., Jordan, T.X., Wessels, H.H., Hoagland, D.A., Kasela, S., Legut, M., Maniatis, S.,
835 Mimitou, E.P., Lu, L., Geller, E., *et al.* (2021). Identification of required host factors for SARS-
836 CoV-2 infection in human cells. *Cell* 184, 92-105 e116.
- 837
- 838 Doan, M., Vorobjev, I., Rees, P., Filby, A., Wolkenhauer, O., Goldfeld, A.E., Lieberman, J.,
839 Barteneva, N., Carpenter, A.E., and Hennig, H. (2018). Diagnostic potential of imaging flow
840 cytometry. *Trends Biotechnol* 36, 649-652.

841
842 Dong, E., Du, H., and Gardner, L. (2020). An interactive web-based dashboard to track COVID-
843 19 in real time. *Lancet Infect Dis* 20, 533-534.
844
845 Doumbo, O., Rossignol, J.F., Pichard, E., Traore, H.A., Dembele, T.M., Diakite, M., Traore, F.,
846 and Diallo, D.A. (1997). Nitazoxanide in the treatment of cryptosporidial diarrhea and other
847 intestinal parasitic infections associated with acquired immunodeficiency syndrome in tropical
848 Africa. *Am J Trop Med Hyg* 56, 637-639.
849
850 Emeny, J.M., and Morgan, M.J. (1979). Regulation of the interferon system: evidence that Vero
851 cells have a genetic defect in interferon production. *J Gen Virol* 43, 247-252.
852
853 Escalera, A., Gonzalez-Reiche, A.S., Aslam, S., Mena, I., Pearl, R.L., Laporte, M., Fossati, A.,
854 Rathnasinghe, R., Alshammery, H., van de Guchte, A., *et al.* (2021). SARS-CoV-2 variants of
855 concern have acquired mutations associated with an increased spike cleavage. *bioRxiv*.
856
857 Feng, Z., Cerveny, M., Yan, Z., and He, B. (2007). The VP35 protein of Ebola virus inhibits the
858 antiviral effect mediated by double-stranded RNA-dependent protein kinase PKR. *J Virol* 81,
859 182-192.
860
861 Gottlieb, R.L., Vaca, C.E., Paredes, R., Mera, J., Webb, B.J., Perez, G., Oguchi, G., Ryan, P.,
862 Nielsen, B.U., Brown, M., *et al.* (2021). Early remdesivir to prevent progression to severe Covid-
863 19 in outpatients. *N Engl J Med* 386, 305-315.
864
865 Haffizulla, J., Hartman, A., Hoppers, M., Resnick, H., Samudrala, S., Ginocchio, C., Bardin, M.,
866 Rossignol, J.F., and Group, U.S.N.I.C.S. (2014). Effect of nitazoxanide in adults and adolescents
867 with acute uncomplicated influenza: a double-blind, randomised, placebo-controlled, phase 2b/3
868 trial. *Lancet Infect Dis* 14, 609-618.
869
870 Haridas, V., Ranjbar, S., Vorobjev, I.A., Goldfeld, A.E., and Barteneva, N.S. (2017). Imaging
871 flow cytometry analysis of intracellular pathogens. *Methods* 112, 91-104.
872
873 Harvey, W.T., Carabelli, A.M., Jackson, B., Gupta, R.K., Thomson, E.C., Harrison, E.M.,
874 Ludden, C., Reeve, R., Rambaut, A., Consortium, C.-G.U., *et al.* (2021). SARS-CoV-2 variants,
875 spike mutations and immune escape. *Nat Rev Microbiol* 19, 409-424.
876
877 Hou, Y.J., Okuda, K., Edwards, C.E., Martinez, D.R., Asakura, T., Dinnon, K.H., 3rd, Kato, T.,
878 Lee, R.E., Yount, B.L., Mascenik, T.M., *et al.* (2020). SARS-CoV-2 reverse genetics reveals a
879 variable infection gradient in the respiratory tract. *Cell* 182, 429-446 e414.
880
881 Huang, J., Hume, A.J., Abo, K.M., Werder, R.B., Villacorta-Martin, C., Alysandratos, K.D.,
882 Beermann, M.L., Simone-Roach, C., Lindstrom-Vautrin, J., Olejnik, J., *et al.* (2020). SARS-
883 CoV-2 infection of pluripotent stem cell-derived human lung Alveolar Type 2 cells elicits a rapid
884 epithelial-intrinsic inflammatory response. *Cell Stem Cell* 27, 962-973 e967.
885

886 Hurley, K., Ding, J., Villacorta-Martin, C., Herriges, M.J., Jacob, A., Vedaie, M., Alysandratos,
887 K.D., Sun, Y.L., Lin, C., Werder, R.B., *et al.* (2020). Reconstructed single-cell fate trajectories
888 define lineage plasticity windows during differentiation of human PSC-derived distal lung
889 progenitors. *Cell Stem Cell* 26, 593-608 e598.
890
891 Hussar, D.A. (2004). New drugs of 2003. *J Am Pharm Assoc* (2003) 44, 168-206; quiz 207-110.
892 Ianevski, A., Giri, A.K., and Aittokallio, T. (2020). SynergyFinder 2.0: visual analytics of multi-
893 drug combination synergies. *Nucleic Acids Res* 48, W488-W493.
894
895 Imai, M., Iwatsuki-Horimoto, K., Hatta, M., Loeber, S., Halfmann, P.J., Nakajima, N.,
896 Watanabe, T., Ujie, M., Takahashi, K., Ito, M., *et al.* (2020). Syrian hamsters as a small animal
897 model for SARS-CoV-2 infection and countermeasure development. *Proc Natl Acad Sci USA*
898 117, 16587-16595.
899
900 Jacob, A., Vedaie, M., Roberts, D.A., Thomas, D.C., Villacorta-Martin, C., Alysandratos, K.D.,
901 Hawkins, F., and Kotton, D.N. (2019). Derivation of self-renewing lung alveolar epithelial type
902 II cells from human pluripotent stem cells. *Nat Protoc* 14, 3303-3332.
903
904 Jasenosky, L.D., Cadena, C., Mire, C.E., Borisevich, V., Haridas, V., Ranjbar, S., Nambu, A.,
905 Bavari, S., Soloveva, V., Sadukhan, S., *et al.* (2019). The FDA-Approved Oral Drug
906 Nitazoxanide Amplifies Host Antiviral Responses and Inhibits Ebola Virus. *iScience* 19, 1279-
907 1290.
908
909 Jayk Bernal, A., Gomes da Silva, M.M., Musungaie, D.B., Kovalchuk, E., Gonzalez, A., Delos
910 Reyes, V., Martin-Quiros, A., Caraco, Y., Williams-Diaz, A., Brown, M.L., *et al.* (2021).
911 Molnupiravir for Oral Treatment of Covid-19 in Nonhospitalized Patients. *N Engl J Med*.
912 Ledford, H. (2021). COVID antiviral pills: what scientists still want to know. *Nature* 599, 358-
913 359.
914
915 Leung, D.W., Ginder, N.D., Fulton, D.B., Nix, J., Basler, C.F., Honzatko, R.B., and
916 Amarasinghe, G.K. (2009). Structure of the Ebola VP35 interferon inhibitory domain. *Proc Natl*
917 *Acad Sci U S A* 106, 411-416.
918
919 Leung, D.W., Prins, K.C., Borek, D.M., Farahbakhsh, M., Tufariello, J.M., Ramanan, P., Nix,
920 J.C., Helgeson, L.A., Otwinowski, Z., Honzatko, R.B., *et al.* (2010). Structural basis for dsRNA
921 recognition and interferon antagonism by Ebola VP35. *Nat Struct Mol Biol* 17, 165-172.
922
923 Leventhal, S.S., Clancy, C., Erasmus, J., Feldmann, H., and Hawman, D.W. (2021). An
924 Intramuscular DNA Vaccine for SARS-CoV-2 Decreases Viral Lung Load but Not Lung
925 Pathology in Syrian Hamsters. *Microorganisms* 9, 1040.
926
927 Loewe, S. (1953). The problem of synergism and antagonism of combined drugs.
928 *Arzneimittelforschung* 3, 285-290.
929

- 930 Matsuyama, S., Nao, N., Shirato, K., Kawase, M., Saito, S., Takayama, I., Nagata, N., Sekizuka,
931 T., Katoh, H., Kato, F., *et al.* (2020). Enhanced isolation of SARS-CoV-2 by TMPRSS2-
932 expressing cells. *Proc Natl Acad Sci USA* *117*, 7001-7003.
- 933
934 Miner, K., Labitzke, K., Liu, B., Wang, P., Henckels, K., Gaida, K., Elliott, R., Chen, J.J., Liu,
935 L., Leith, A., *et al.* (2019). Drug repurposing: the anthelmintics niclosamide and nitazoxanide are
936 potent TMEM16A antagonists that fully bronchodilate airways. *Front Pharmacol* *10*, 51.
- 937
938 Miorin, L., Kehrer, T., Sanchez-Aparicio, M.T., Zhang, K., Cohen, P., Patel, R.S., Cupic, A.,
939 Makio, T., Mei, M., Moreno, E., *et al.* (2020). SARS-CoV-2 Orf6 hijacks Nup98 to block STAT
940 nuclear import and antagonize interferon signaling. *Proc Natl Acad Sci U S A* *117*, 28344-
941 28354.
- 942
943 Osada, N., Kohara, A., Yamaji, T., Hirayama, N., Kasai, F., Sekizuka, T., Kuroda, M., and
944 Hanada, K. (2014). The genome landscape of the African green monkey kidney-derived vero cell
945 line. *DNA Res* *21*, 673-683.
- 946
947 Piacentini, S., La Frazia, S., Riccio, A., Pedersen, J.Z., Topai, A., Nicolotti, O., Rossignol, J.F.,
948 and Santoro, M.G. (2018). Nitazoxanide inhibits paramyxovirus replication by targeting the
949 Fusion protein folding: role of glycoprotein-specific thiol oxidoreductase ERp57. *Sci Rep* *8*,
950 10425.
- 951
952 Pruijssers, A.J., George, A.S., Schafer, A., Leist, S.R., Gralinski, L.E., Dinnon, K.H., 3rd, Yount,
953 B.L., Agostini, M.L., Stevens, L.J., Chappell, J.D., *et al.* (2020). Remdesivir Inhibits SARS-
954 CoV-2 in Human Lung Cells and Chimeric SARS-CoV Expressing the SARS-CoV-2 RNA
955 Polymerase in Mice. *Cell Rep* *32*, 107940.
- 956
957 Ranjbar, S., Haridas, V., Nambu, A., Jasenosky, L.D., Sadhukhan, S., Ebert, T.S., Hornung, V.,
958 Cassell, G.H., Falvo, J.V., and Goldfeld, A.E. (2019). Cytoplasmic RNA Sensor Pathways and
959 Nitazoxanide Broadly Inhibit Intracellular *Mycobacterium tuberculosis* Growth. *iScience* *22*,
960 299-313.
- 961
962 Reid, S.P., Leung, L.W., Hartman, A.L., Martinez, O., Shaw, M.L., Carbonnelle, C., Volchkov,
963 V.E., Nichol, S.T., and Basler, C.F. (2006). Ebola virus VP24 binds karyopherin α 1 and blocks
964 STAT1 nuclear accumulation. *J Virol* *80*, 5156-5167.
- 965
966 Reid, S.P., Valmas, C., Martinez, O., Sanchez, F.M., and Basler, C.F. (2007). Ebola virus VP24
967 proteins inhibit the interaction of NPI-1 subfamily karyopherin α proteins with activated STAT1.
968 *J Virol* *81*, 13469-13477.
- 969
970 Riva, L., Yuan, S., Yin, X., Martin-Sancho, L., Matsunaga, N., Pache, L., Burgstaller-
971 Muehlbacher, S., De Jesus, P.D., Teriete, P., Hull, M.V., *et al.* (2020). Discovery of SARS-CoV-
972 2 antiviral drugs through large-scale compound repurposing. *Nature* *586*, 113-119.
- 973
974 Rossignol, J.-F. (2014). Nitazoxanide: a first-in-class broad-spectrum antiviral agent. *Antiviral*
975 *Res* *110*, 94-103.

976
977 Rossignol, J.-F., Matthew, C.B., Oaks, J.B., Bostick, G., Vora, K.N., Fulgencio, J., Mogelnicki,
978 D., Bréchet, C., and Vanguard Study Group (2021). Early treatment with nitazoxanide prevents
979 worsening of mild and moderate COVID-19 and subsequent hospitalization. medRxiv.
980
981 Rossignol, J.F., Hidalgo, H., Feregrino, M., Higuera, F., Gomez, W.H., Romero, J.L., Padierna,
982 J., Geyne, A., and Ayers, M.S. (1998). A double-'blind' placebo-controlled study of nitazoxanide
983 in the treatment of cryptosporidial diarrhoea in AIDS patients in Mexico. *Trans R Soc Trop Med*
984 *Hyg* 92, 663-666.
985
986 Rossignol, J.F., La Frazia, S., Chiappa, L., Ciucci, A., and Santoro, M.G. (2009). Thiazolidines, a
987 new class of anti-influenza molecules targeting viral hemagglutinin at the post-translational
988 level. *J Biol Chem* 284, 29798-29808.
989
990 Sampaio, N.G., Chauveau, L., Hertzog, J., Bridgeman, A., Fowler, G., Moonen, J.P., Dupont,
991 M., Russell, R.A., Noerenberg, M., and Rehwinkel, J. (2021). The RNA sensor MDA5 detects
992 SARS-CoV-2 infection. *Sci Rep* 11, 13638.
993
994 Schroeder, B.C., Cheng, T., Jan, Y.N., and Jan, L.Y. (2008). Expression cloning of TMEM16A
995 as a calcium-activated chloride channel subunit. *Cell* 134, 1019-1029.
996
997 Schumann, M., Gantke, T., and Muhlberger, E. (2009). Ebola virus VP35 antagonizes PKR
998 activity through its C-terminal interferon inhibitory domain. *J Virol* 83, 8993-8997.
999
1000 Sia, S.F., Yan, L.-M., Chin, A.W.H., Fung, K., Poon, L.L.M., Nicholls, J.M., Peiris, M., and
1001 Yen, H.-L. (2020). Pathogenesis and transmission of SARS-CoV-2 virus in golden Syrian
1002 hamsters. *Nature* 583, 834-838.
1003
1004 Stachulski, A.V., Rossignol, J.F., Pate, S., Taujanskas, J., Robertson, C.M., Aerts, R., Pascal, E.,
1005 Piacentini, S., Frazia, S., Santoro, M.G., *et al.* (2021). Synthesis, antiviral activity, preliminary
1006 pharmacokinetics and structural parameters of thiazolide amine salts. *Future Med Chem* 13,
1007 1731-1741.
1008
1009 Wang, M., Cao, R., Zhang, L., Yang, X., Liu, J., Xu, M., Shi, Z., Hu, Z., Zhong, W., and Xiao,
1010 G. (2020). Remdesivir and chloroquine effectively inhibit the recently emerged novel
1011 coronavirus (2019-nCoV) in vitro. *Cell Res* 30, 269-271.
1012
1013 White, K.M., Rosales, R., Yildiz, S., Kehrer, T., Miorin, L., Moreno, E., Jangra, S., Uccellini,
1014 M.B., Rathnasinghe, R., Coughlan, L., *et al.* (2021). Plitidepsin has potent preclinical efficacy
1015 against SARS-CoV-2 by targeting the host protein eEF1A. *Science* 371, 926-931.
1016
1017 Xie, X., Muruato, A., Lokugamage, K.G., Narayanan, K., Zhang, X., Zou, J., Liu, J.,
1018 Schindewolf, C., Bopp, N.E., Aguilar, P.V., *et al.* (2020). An Infectious cDNA Clone of SARS-
1019 CoV-2. *Cell Host Microbe* 27, 841-848 e843.
1020

- 1021 Xu, W., Edwards, M.R., Borek, D.M., Feagins, A.R., Mittal, A., Alinger, J.B., Berry, K.N., Yen,
1022 B., Hamilton, J., Brett, T.J., *et al.* (2014). Ebola virus VP24 targets a unique NLS binding site on
1023 karyopherin alpha 5 to selectively compete with nuclear import of phosphorylated STAT1. *Cell*
1024 *Host Microbe* *16*, 187-200.
- 1025
1026 Yang, Y.D., Cho, H., Koo, J.Y., Tak, M.H., Cho, Y., Shim, W.S., Park, S.P., Lee, J., Lee, B.,
1027 Kim, B.M., *et al.* (2008). TMEM16A confers receptor-activated calcium-dependent chloride
1028 conductance. *Nature* *455*, 1210-1215.
- 1029
1030 Yin, X., Riva, L., Pu, Y., Martin-Sancho, L., Kanamune, J., Yamamoto, Y., Sakai, K., Gotoh, S.,
1031 Miorin, L., De Jesus, P.D., *et al.* (2021). MDA5 governs the innate immune response to SARS-
1032 CoV-2 in lung epithelial cells. *Cell Rep* *34*, 108628.
- 1033
1034 Zhang, A.P., Bornholdt, Z.A., Liu, T., Abelson, D.M., Lee, D.E., Li, S., Woods, V.L., Jr., and
1035 Saphire, E.O. (2012). The ebola virus interferon antagonist VP24 directly binds STAT1 and has
1036 a novel, pyramidal fold. *PLoS Pathog* *8*, e1002550.
- 1037

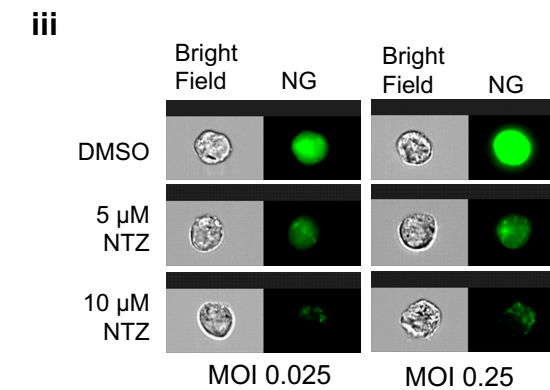
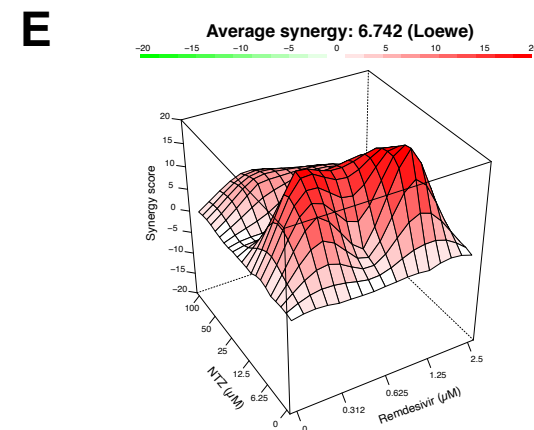
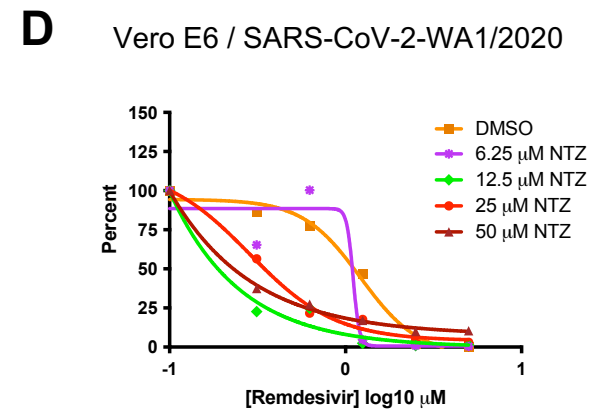
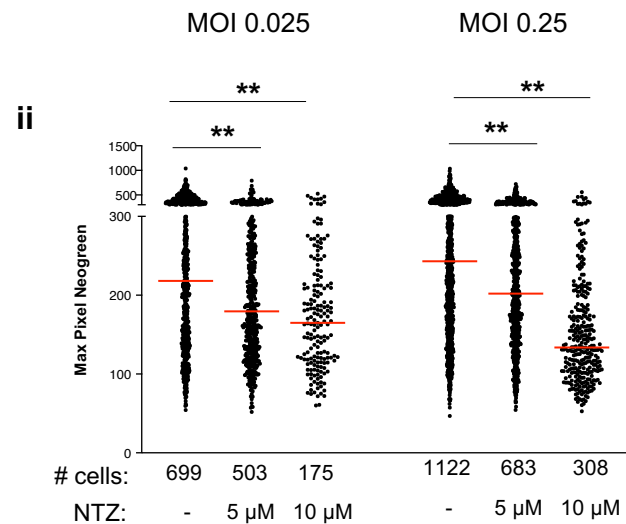
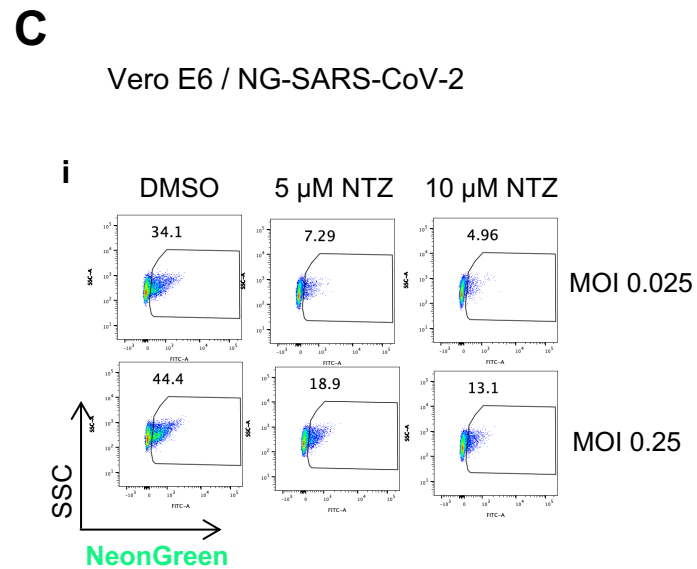
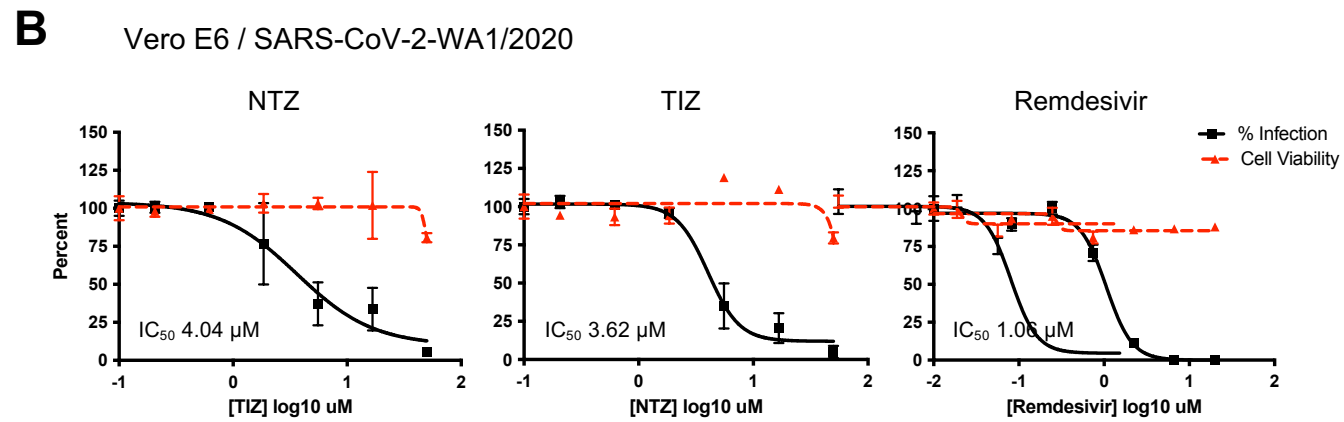
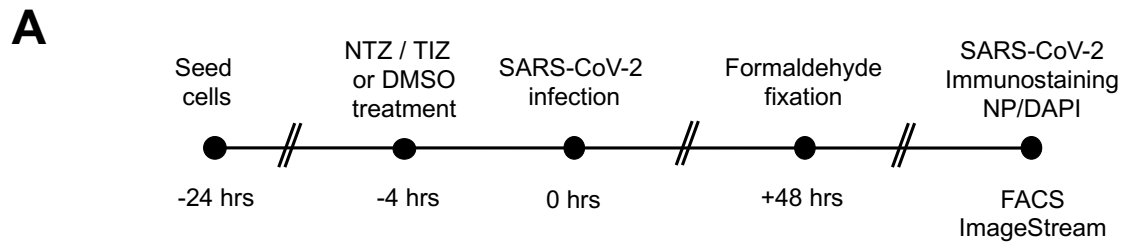
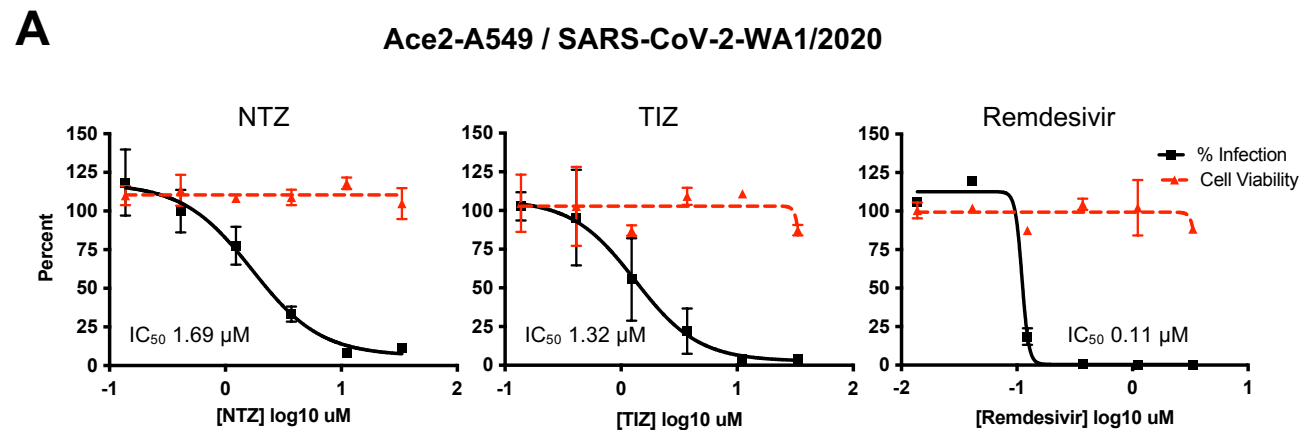
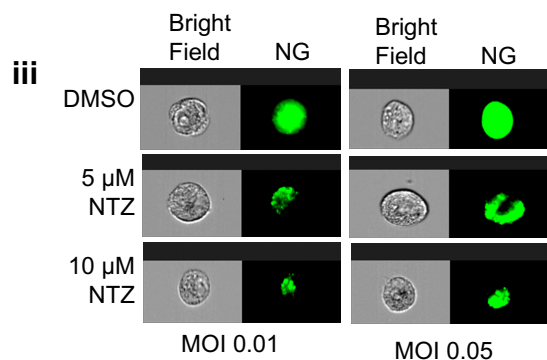
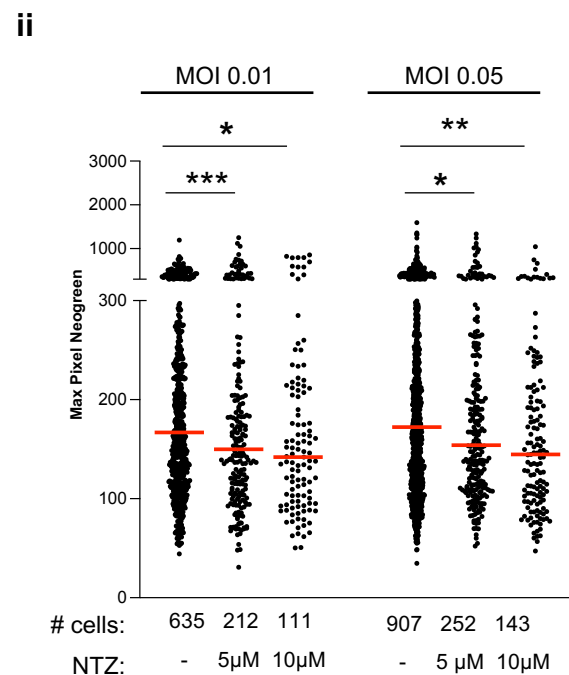
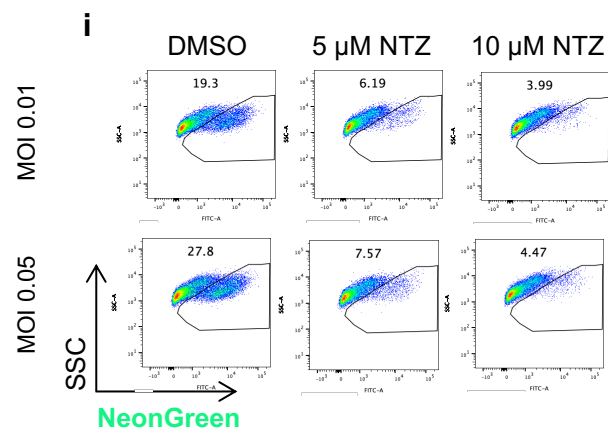


Fig. 1



B Ace2-A549 / Neon-Green-SARS-CoV-2



C Ace2-A549 WT and IFNAR-KO / Neon-Green-SARS-CoV-2

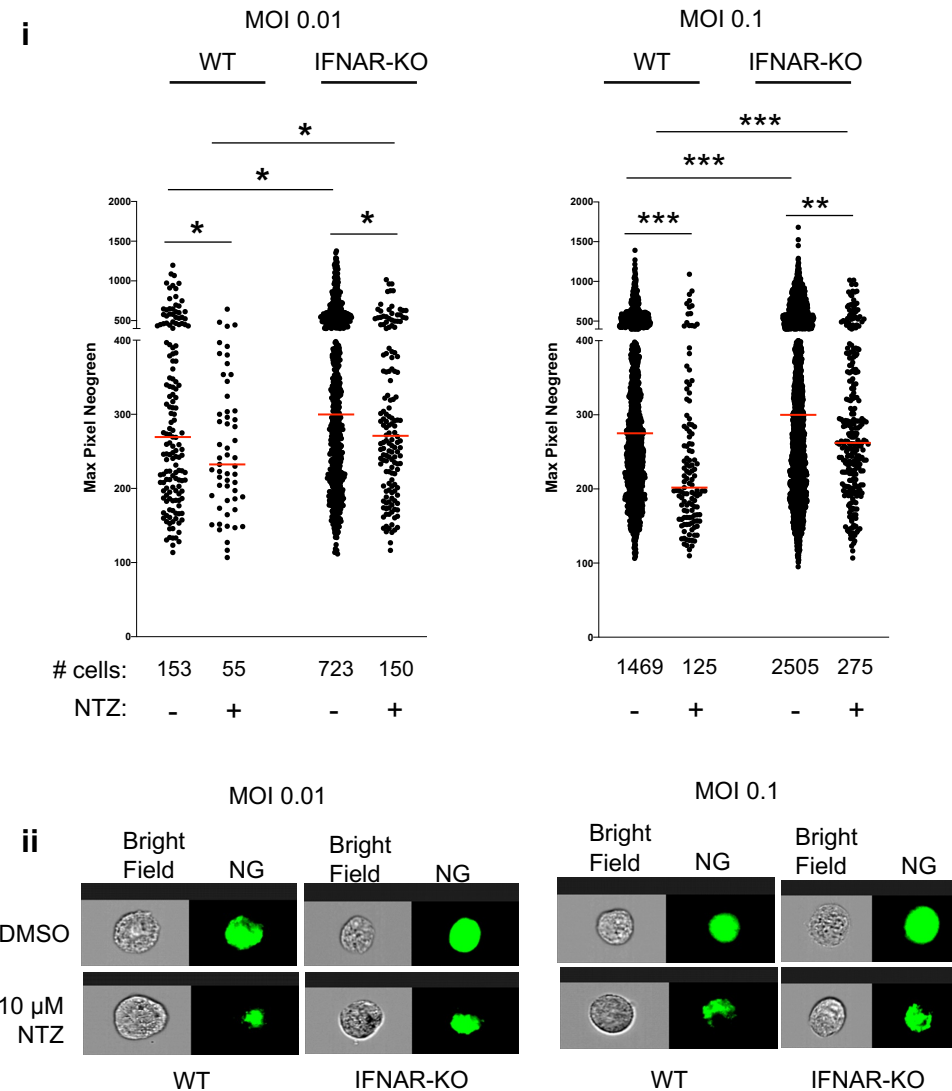
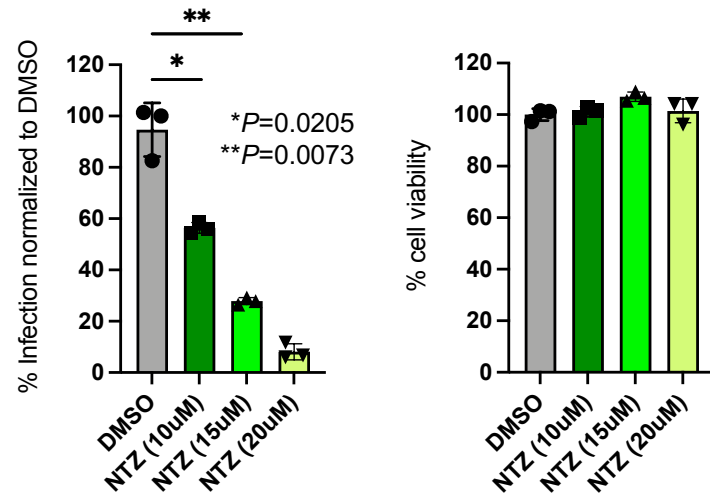
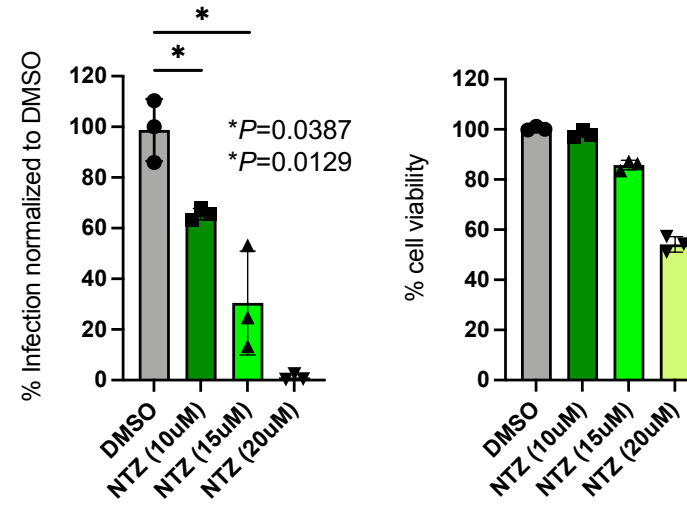
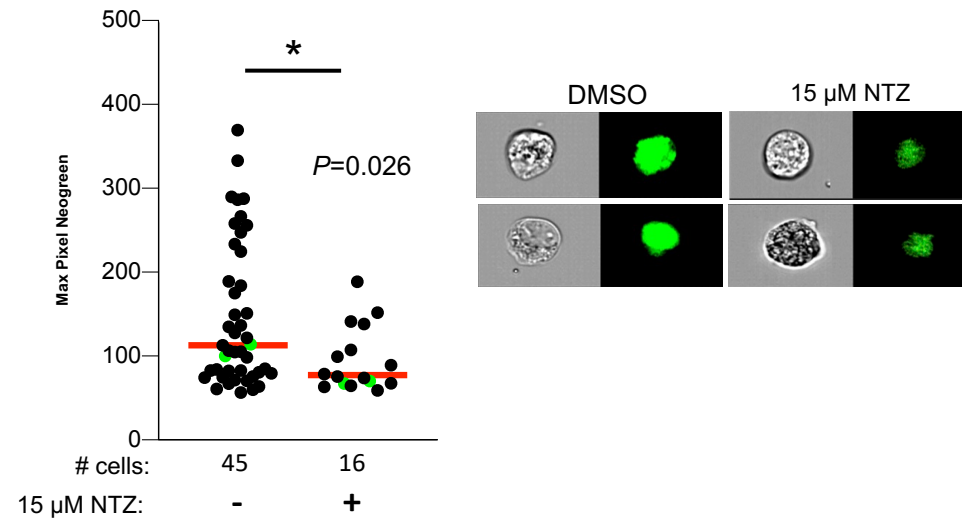


Fig. 2

A**H9 cells / SARS-CoV-2-WA1/2020****B****iAT2 cells / SARS-CoV-2-WA1/2020****C****iAT2 cells / NG-SARS-CoV-2****Fig. 3**

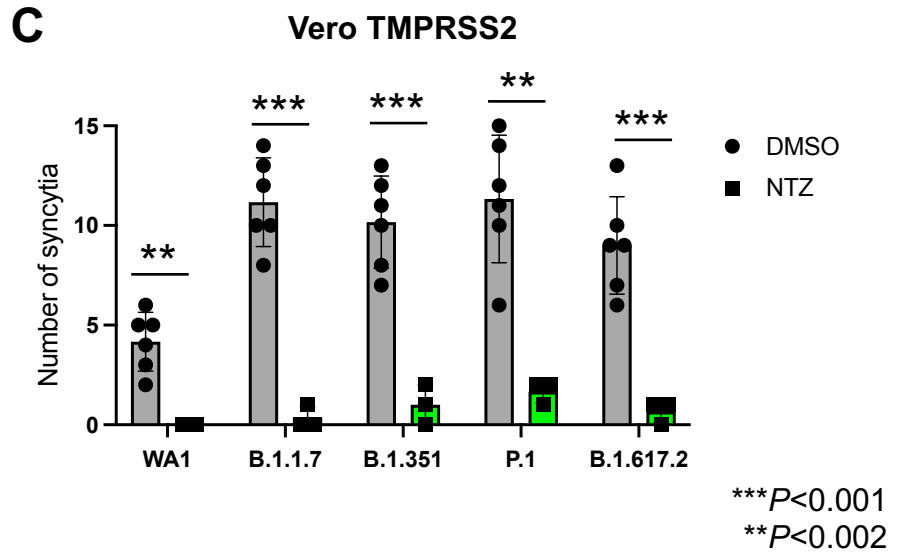
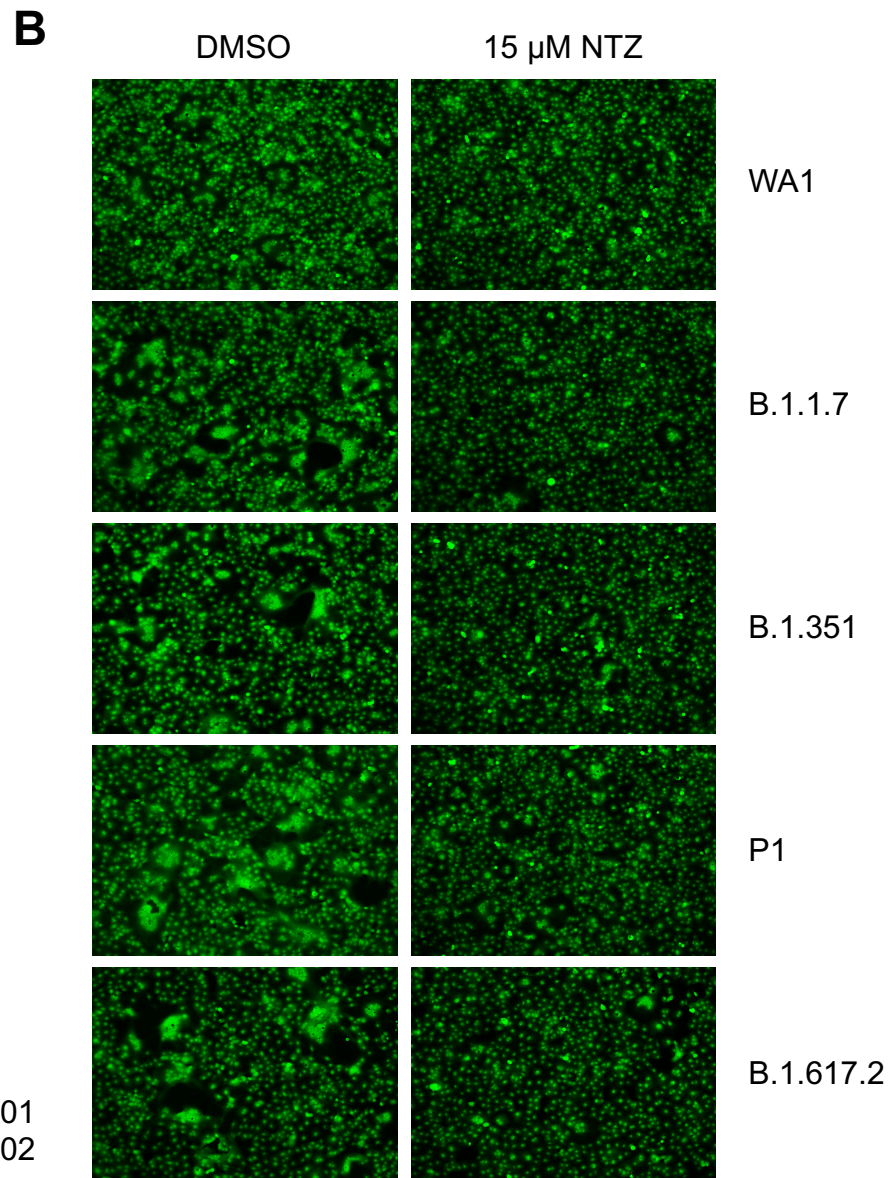
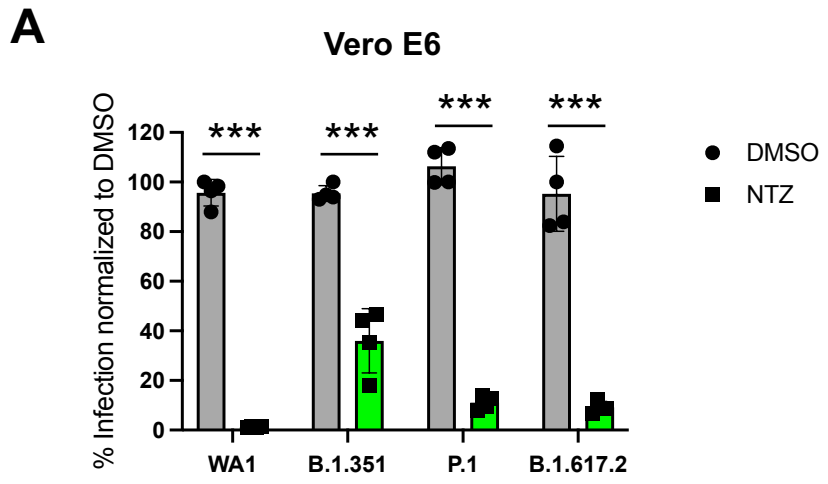


Fig. 4

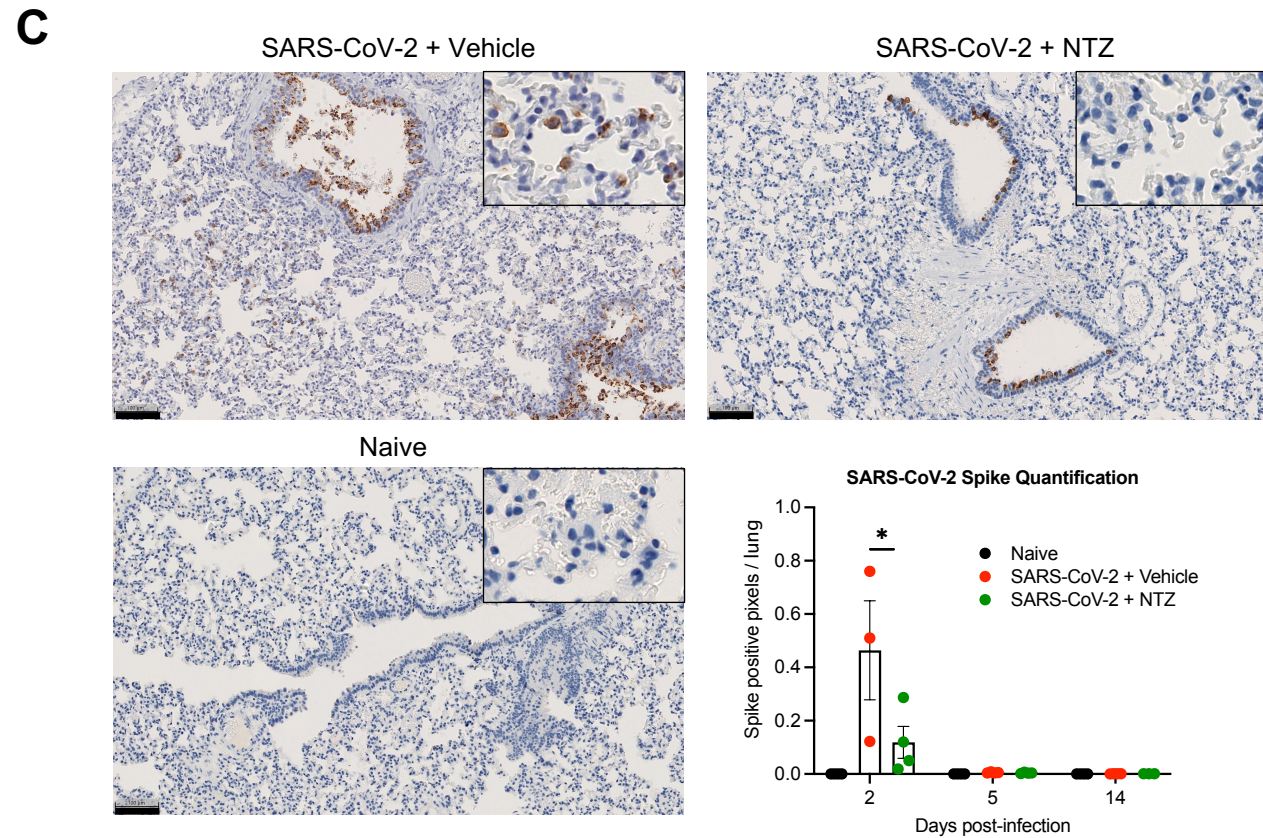
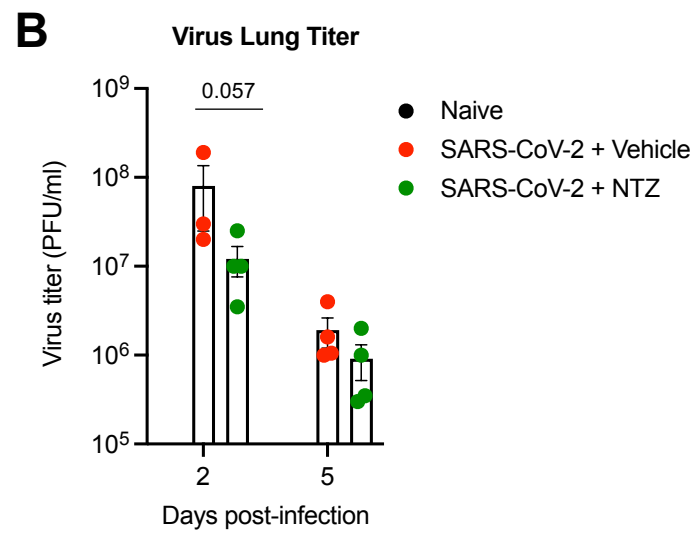
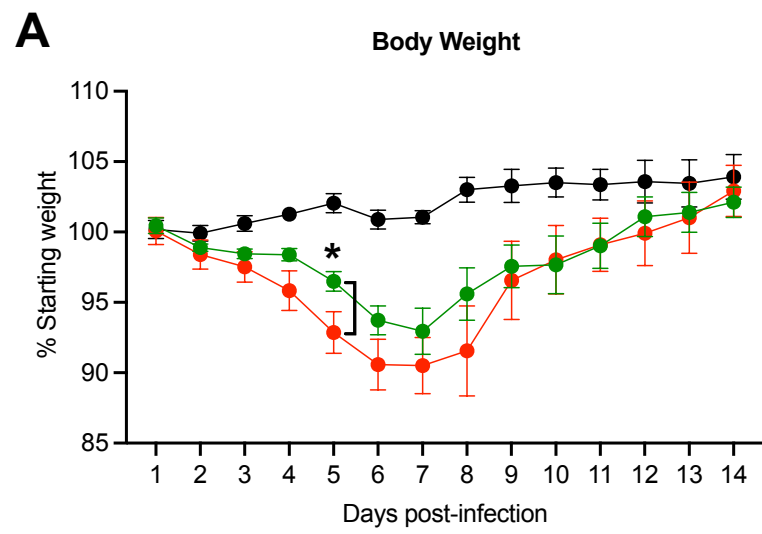


Fig. 5

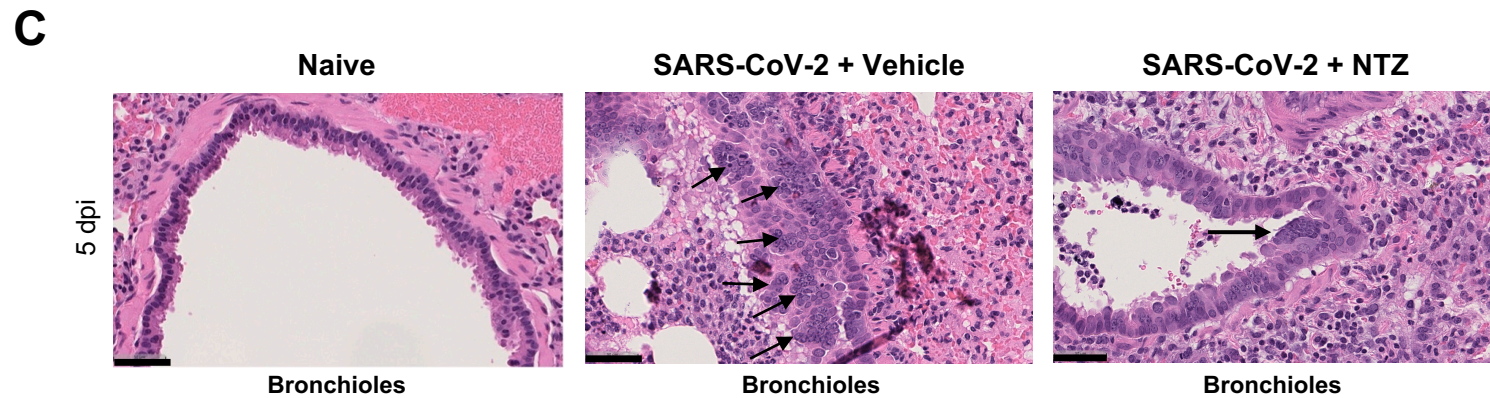
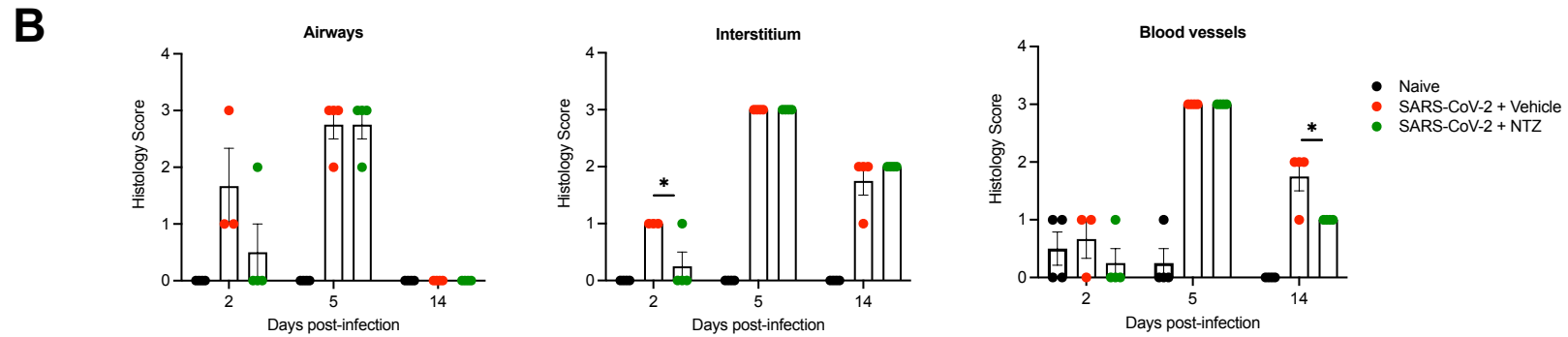
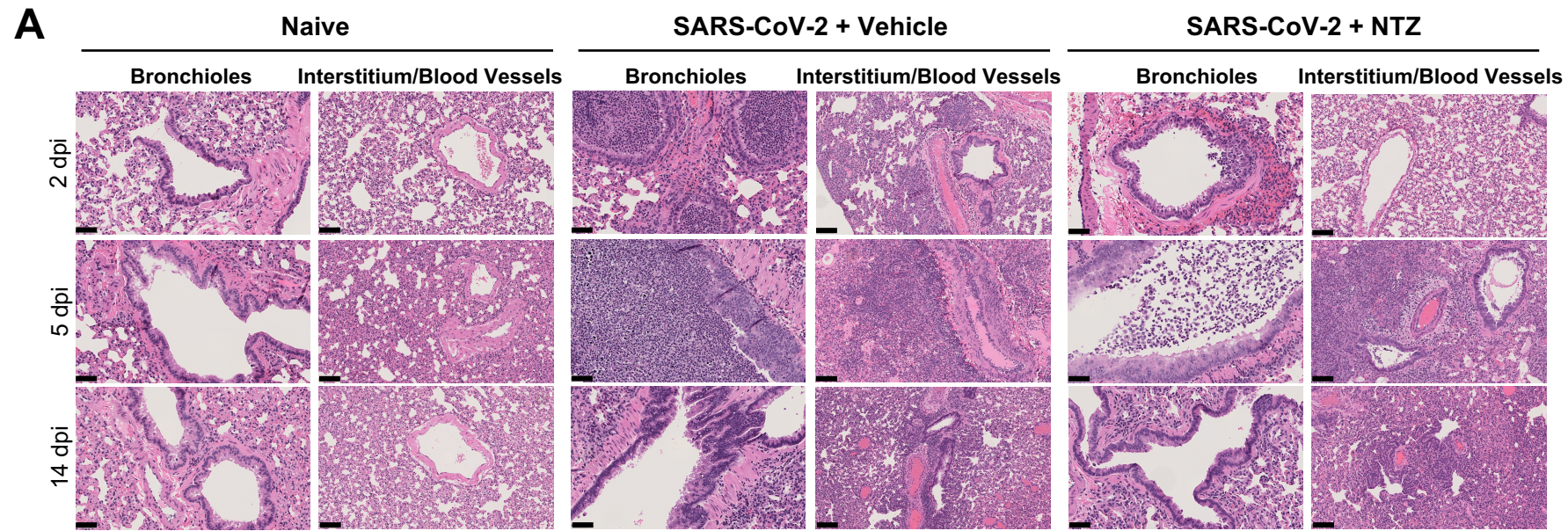


Fig. 6